Bispecific Targeting of Conserved Epitopes Enables Pan-Hantavirus Neutralization

Jiayao Yang[1,4,10], Zihao Jiang[6,7,10], Yudun Ke[1,10], Xuyang Zheng[8,10], Ziyu Liu[9,10], Shuliang Chen[6,7], Lijuan Niu[6,7], Fan Luo[6,7], Ziniu Dai[1], Jinhao Bi[1], Mingxi Li[1], Xiao Dang[8], Jiayi Shu[5], Fajie Yuan[3], Zeli Zhang[1,2], Zhiqiang Ku[1,2], Ren Sun[1,2], Xingan Wu[9], Jianqi Lian[8], Rongrong Liu[9,11], Wei Hou[6,7,11], Zhaoqian Wang[1,2,11], Dapeng Li[1,2,11]

[1]Center for Infectious Disease Research, Zhejiang Key Laboratory of Multi-Omics in Infection and Immunity, School of Medicine; [2]School of Life Sciences; [3]School of Engineering, Westlake University, Hangzhou, Zhejiang 310024, China.

[4]School of Life Sciences, [5]Clinical Center for Biotherapy, Zhongshan Hospital & Zhongshan Hospital (Xiamen), Fudan University, Shanghai, China.

[6]State Key Laboratory of Virology and Biosafety, Hubei Province Key Laboratory of Allergy and Immunology, Institute of Medical Virology, Taikang Medical School (School of Basic Medical Sciences), Wuhan University, Wuhan, Hubei 430071, China.

[7]Shenzhen Research Institute, Wuhan University, Shenzhen, Guangdong 518057, China.

[8]Department of Infectious Diseases, Tangdu Hospital; [9]Department of Microbiology, School of Basic Medicine, Fourth Military Medical University, Xi'an, Shaanxi 710038, China.

[10]Co-first Authors

[11]Corresponding Authors

Correspondence: Rongrong Liu (liurongrong@fmmu.edu.cn), Wei Hou (houwei@whu.edu.cn), Zhaoqian Wang (wangzhaoqian@westlake.edu.cn) and Dapeng Li (lidapeng@westlake.edu.cn)

ABSTRACT

Hantaviruses cause renal and cardiopulmonary syndromes with case-fatality rates up to 40%, yet no approved antiviral therapy exists. Antigenic divergence between Old World and New World hantaviruses has impeded the development of broadly protective antibody therapeutics. Here, we isolated neutralizing antibodies from convalescent donors and identified two lead antibodies targeting distinct conserved epitopes. XA-3H12 potently neutralizes Old World hantaviruses, whereas XA-044 broadly neutralizes HTNV, SNV and ANDV. Cryo-EM structures revealed that XA-044 recognizes the apical Gn-Gc interface, whereas XA-3H12 binds the basal region of Gc domain II, defining two non-overlapping conserved neutralization sites. Guided by these structures, we engineered a bispecific IgG-scFv that integrates the breadth and potency of both parental antibodies and achieves broad hantavirus neutralization. In mouse models, the IgG-scFv blocked entry of diverse hantavirus pseudoviruses *in vivo* and conferred post-exposure protection against lethal HTNV challenge, establishing a dual-epitope bispecific antibody candidate for broad hantavirus intervention.

INTRODUCTION

Hantaviruses are enveloped, segmented, negative-sense RNA viruses of the order *Bunyavirales*, broadly classified into Old World and New World lineages according to their geographic distribution and associated disease manifestations [1-3]. Old World hantaviruses (OWH), including Hantaan virus (HTNV), Seoul virus (SEOV), Puumala virus (PUUV), and Dobrava-Belgrade virus (DOBV), circulate predominantly in Europe and Asia and cause hemorrhagic fever with renal syndrome (HFRS), with case-fatality rates ranging from 1% to 15% [4-6]. In contrast, New World hantaviruses (NWH), such as Andes virus (ANDV) and Sin Nombre virus (SNV), are endemic to the Americas and cause hantavirus cardiopulmonary syndrome (HCPS), a severe respiratory disease with fatality rates approaching 40% [4,7,8]. Rodents serve as the natural reservoirs, and human infection occurs primarily through inhalation of aerosolized virus-contaminated excreta [9]. Despite the substantial morbidity and mortality associated with hantavirus infections, no FDA-approved antiviral therapies are currently available [6,10]. Clinical management remains largely supportive, underscoring the urgent need for effective prophylactic and therapeutic countermeasures.

The hantavirus genome comprises three segments—small (S), medium (M), and large (L)—which encode the nucleocapsid protein (NP), the glycoprotein precursor (GPC), and the RNA-dependent RNA polymerase (RdRp), respectively [11]. The GPC is processed by host signal peptidase into two surface glycoproteins, Gn and Gc, which assemble into tetrameric, square-shaped $(Gn/Gc)_4$ on the virion surface [12,13]. These glycoproteins mediate viral attachment, endosomal entry, and membrane fusion, and constitute the principal targets of the host neutralizing antibody response [14-19]. Accordingly, Gn and Gc represent the most attractive antigens for vaccine design and antibody-based therapeutic development.

Although antibody-based countermeasures hold considerable promise, developing a broadly protective therapeutic capable of addressing the extensive antigenic diversity of hantaviruses remains a major challenge. Previously identified monoclonal antibodies have demonstrated encouraging activity, but important gaps remain. For example, neutralizing antibodies isolated from convalescent donors protected against NWH, yet their neutralizing capacity against major HFRS-causing viruses such as HTNV and SEOV was not defined, and the lack of epitope mapping limited mechanistic understanding [3,18]. More recently, the broadly

neutralizing antibody ADI-42898, isolated from a PUUV-infected individual [20,21], representing an important conceptual advance for the development of pan-hantavirus antibody countermeasures. However, ADI-42898 showed relatively limited neutralizing potency against several clinically important hantaviruses, including HTNV, and its activity relies on recognition of a single conserved epitope. Thus, antibody-based therapeutics that achieve broad-spectrum neutralization by simultaneously targeting two distinct conserved epitopes—and thereby may reduce the likelihood of viral escape—remain an important unmet need.

Here, we address this gap by isolating and characterizing a panel of potent neutralizing antibodies from four HFRS convalescent donors. From this panel, we identified two lead antibodies with distinct neutralization profiles: XA-3H12, a highly potent neutralizer of the OWHs HTNV and SEOV, and XA-044, a broadly reactive antibody that neutralizes HTNV as well as the NWHs SNV and ANDV. Cryo-EM analyses revealed that these antibodies recognize two non-overlapping conserved epitopes on the hantavirus Gn-Gc glycoprotein complex, providing a structural basis for their neutralizing activities. Guided by these findings, we evaluated multiple bispecific antibody formats and identified an IgG-scFv derivative with the strongest breadth and potency. This bispecific antibody achieved broad-spectrum neutralization across OWHs and NWHs, blocked viral entry *in vivo* in a bioluminescent vesicular stomatitis virus (VSV)-pseudotyped hantavirus reporter system, and provided robust post-exposure protection in a lethal HTNV mouse challenge model. Together, these findings establish a dual-epitope bispecific antibody as a promising pan-hantavirus therapeutic candidate and provide structural guidance for the rational design of next-generation hantavirus vaccines.

RESULTS

Isolation of cross-reactive antibodies from HFRS convalescent patients

We collected blood samples from four individuals who had recovered from HFRS. Plasma from all four donors showed strong binding to HTNV and SEOV Gn and Gc antigens (***Extended Data Fig. 1a,b***). To assess cross-reactive neutralizing activity against both OWH and NWH, we used recombinant VSV pseudoviruses (rVSV) bearing the Gn-Gc glycoproteins of HTNV, SEOV, SNV, and ANDV [22,23]. Donor plasma exhibited broad and potent

neutralization of OWH pseudoviruses, whereas neutralization of NWH pseudoviruses was variable but detectable (***Fig.1a***).

To isolate antigen-specific memory B cells, peripheral blood mononuclear cells (PBMCs) were sorted using biotinylated HTNV and SEOV Gn and Gc proteins as probes, followed by single-cell PCR amplification or single-cell B-cell receptor sequencing (scBCR-seq) (***Fig.1b and Extended Data Fig. 1c***). We sorted 384 Gn/Gc-specific single B cells and recovered 323 paired heavy- and light-chain sequences for recombinant IgG expression. An additional 68 paired sequences were selected for synthesis based on somatic hypermutation (SHM) rates and complementarity-determining region 3 (CDR3) lengths. Screening of the resulting recombinant antibodies against Gn and Gc from HTNV, SEOV, SNV, and ANDV identified 117 antibodies reactive with at least one virus (***Extended Data Table 1***). The mean SHM rates of the heavy and light chains were 7.9% and 5.3%, respectively (***Fig. 1c***), and the mean CDR3 lengths were 18 and 10 amino acids, respectively (***Fig. 1d***). Among these antibodies, 9 Gn-directed and 21 Gc-directed antibodies displayed cross-reactivity across multiple viruses. Gn cross-reactive antibodies were largely restricted to OWH, whereas Gc-directed antibodies exhibited broader reactivity, including strong binding to NWH Gc (***Fig. 1e***). Collectively, these data demonstrate that cross-reactive antibodies targeting diverse hantaviruses exist in HFRS convalescent donors.

Identification of NAbs targeting distinct hantavirus Gn/Gc neutralization sites

We next screened Gn/Gc-specific antibodies for binding to the Gn head domain and Gc ectodomain (***Fig. 2a***), and for neutralizing activity against rVSV-HTNV (***Extended Data Table 1***). Fifteen NAbs, including 10 derived from single-cell PCR and 5 from scBCR-seq, were selected for further characterization (***Extended Data Fig. 2a***). Binding was assessed against isolated Gn head, Gc ectodomain, and a heterodimeric $Gn^{H}Gc$ construct that recapitulates the native quaternary architecture of hantavirus glycoproteins (***Fig. 2b***) [12]. Most antibodies preferentially recognized OWH antigens, with limited binding to NWH glycoproteins (***Fig. 2c and Extended Data Fig. 2b, c***). Several antibodies, including XA-1A5, XA-1D4, XA-044, and XA-060, bound weakly to isolated Gn or Gc but recognized $Gn^{H}Gc$, indicating

conformation-dependent epitopes. Notably, XA-044 was the only antibody that strongly bound NWH $Gn^{H}Gc$, recognizing HTNV, SNV, and ANDV, but not SEOV.

Neutralization assays against OWH and NWH pseudoviruses showed that 12 antibodies potently neutralized rVSV-HTNV, with IC_{50} values below 0.01 μg/mL, whereas three showed moderate activity. Five antibodies—XA-3A8, XA-3H12, XA-4E4, XA-4G11, and XA-058—cross-neutralized rVSV-HTNV and rVSV-SEOV (***Fig. 2d and Extended Data Fig. 2d***). Consistent with its binding profile, XA-044 potently neutralized HTNV, SNV, and ANDV pseudoviruses, but not SEOV. Five antibodies also neutralized authentic HTNV, among which XA-3H12 and XA-044 were the most potent, with IC_{50} values of 0.034 and 0.013 μg/mL, respectively (***Fig. 2d and Extended Data Fig. 2e***).

To map the antigenic landscape, we performed Biolayer Interferometry (BLI)-based competition assays using HTNV glycoproteins. The 15 NAbs segregated into five antigenic sites, A1, A2, B, C, and D (***Fig. 2e and Extended Data Fig. 3***). Site A1, targeted by XA-044, represented a conserved epitope shared by HTNV, SNV, and ANDV, whereas site C targeted by XA-3H12 defined a major OWH neutralizing site. Sites B and D were primarily associated with OWH Gn- and Gc-directed antibodies, respectively. These data reveal multiple neutralizing vulnerabilities on hantavirus $Gn^{H}Gc$ with distinct breadth profiles.

Structural basis of broad neutralization by XA-044 and XA-3H12

Having identified XA-044 and XA-3H12 as two of the most potent NAbs targeting distinct antigenic sites with complementary breadth profiles—site A1 and site C, respectively—we next sought to define the structural basis of their recognition and neutralization. We therefore determined the structures of XA-044 Fab bound to SNV $Gn^{H}Gc$ and XA-3H12 Fab bound to HTNV $Gn^{H}Gc$ (***Extended Data Table 2***). Superposition onto the ANDV Gn-Gc dimer (PDB: 9P3X) [13] showed that XA-044 targets the apical Gn-Gc interface, whereas XA-3H12 binds the basal region of Gc domain II (***Fig. 3a***). XA-044 buries >720 $Å^2$ of surface area through shape complementarity and seven hydrogen bonds, using CDR L1-2 and H3 to contact SNV Gn residues 73-79 and Gc residues 90-92, 129-130, 91-93, 110-115, 129 and 131 (***Fig. 3b,d***). Its epitope partially overlaps that of ADI-65534 [13,21], but is shifted toward the Gc fusion-loop region while retaining Gn capping-loop contacts (***Extended Data Fig. 4a***). In

158 contrast, XA-3H12 buries >1025 Å² on HTNV Gc alone through shape complementarity, hy-
159 drogen bonds and salt bridges mediated by CDR L1, L3, H1-3 and FR3, contacting residues
160 67-72, 147-150, 152, 194-195, 216-219, 225-238 (except 227 and 229), and 288-289; the
161 heavy chain forms eight hydrogen bonds and two salt bridges, and the light chain forms three
162 hydrogen bonds (***Fig. 3e,g***). Notably, N-glycosylation protruded from N328 of HTNV Gn
163 may also stabilize XA-3H12 binding (***Extended Data Fig. 4b***).
164 Conservation analysis showed that 9/13 XA-044 epitope residues on SNV Gc are fully
165 conserved and 13/13 are >70% conserved across OWHs and NWHs, whereas 6/7 Gn residues
166 are >50% conserved; for XA-3H12, 10/31 epitope residues on HTNV Gc are fully conserved
167 and 25/31 are >50% conserved (***Fig. 3h,i***). Structural superposition onto the ANDV Gn-Gc
168 tetramer (PDB: 9P3Y) [13] revealed no clash within a single tetramer, but in the tetramer-dimer
169 interface XA-044 shows minor or no clash with neighboring Gc, whereas XA-3H12 exhibits a
170 major clash with neighboring Gn (***Fig. 3j and Extended Data Fig. 4c,d***). Together, these
171 structures identify two spatially distinct and conserved neutralizing epitopes on the hantavirus
172 Gn-Gc complex that underlie the complementary neutralization profiles of XA-044 and XA-
173 3H12. The non-overlapping binding modes, together with their distinct breadth and potency,
174 provided a structural rationale for combining these antibodies and for engineering bispecific
175 formats capable of simultaneously engaging both neutralizing sites.
176
177 **Bispecific antibody strategies achieve pan-hantavirus neutralization**
178 Guided by the structural demonstration that XA-044 and XA-3H12 recognize spatially
179 distinct and conserved neutralizing epitopes, and by their complementary neutralization
180 breadth, we next asked whether co-targeting these two sites could enhance potency and ex-
181 pand hantavirus coverage. We therefore performed BLI analyses to characterize the binding
182 profiles of XA-044 and XA-3H12 against representative OWH and NWH $Gn^{H}Gc$ antigens.
183 XA-3H12 bound HTNV, SEOV, and SNV $Gn^{H}Gc$ with picomolar to subpicomolar affinities,
184 whereas XA-044 bound ANDV $Gn^{H}Gc$ with subpicomolar affinity (K_D < 1 pM) and also
185 showed high-affinity binding to HTNV and SNV $Gn^{H}Gc$, but not SEOV (***Fig. 4a and Ex-***
186 ***tended Data Fig. 5a***). Consistent with the structural analysis, BLI-based competition assays
187 confirmed that XA-044 and XA-3H12 can simultaneously engage $Gn^{H}Gc$ without detectable

competition, supporting their combined use (***Fig. 4b***). We next assessed whether these two antibodies act synergistically in neutralization. In a checkerboard assay spanning concentrations around their individual IC_{50} values, the XA-044/XA-3H12 cocktail achieved 91.67% neutralization at the combined IC_{50} concentration, exceeding the 75% expected from simple additivity (***Fig. 4c***). These results indicate that co-targeting both neutralization sites produces synergistic enhancement of neutralization potency.

To identify an optimal combinatorial format, we evaluated five designs: a two-antibody cocktail, Knob-into-Hole, CrossMab, Fab-scFv, and IgG-scFv. All formats potently neutralized HTNV, with the cocktail, Fab-scFv, and IgG-scFv achieving IC_{50} values below 1 ng/mL (***Fig. 4d and Extended Data Fig. 5b***). However, Knob-into-Hole, CrossMab, and Fab-scFv showed reduced activity against NWH pseudoviruses, including SNV, ANDV, JUQV, and LNV. By contrast, the cocktail and IgG-scFv preserved the breadth and potency of both parental antibodies, with IC_{50} values comparable to those of XA-044 or XA-3H12 alone (***Fig. 4d and Extended Data Fig. 5b***). Consistently, cell-surface staining of cells expressing full-length viral glycoproteins showed that IgG-scFv combined the binding breadth of both parental antibodies. Whereas XA-3H12 and XA-044 each displayed more restricted binding profiles, IgG-scFv recognized all tested viruses bound by either antibody, including the OWHs HTNV, SEOV, DOBV, and PUUV, as well as the NWHs SNV, ANDV, LNV, JUQV, and CHOV (***Fig. 4e,f and Extended Data Fig. 5c***). Together, these *in vitro* binding and neutralization data demonstrate that the structurally guided IgG-scFv design successfully integrates the complementary breadth and potency of XA-044 and XA-3H12 into a single bispecific molecule. Thus, we advanced the IgG-scFv for subsequent *in vivo* evaluation, with the parental-antibody cocktail included as a benchmark comparator.

A pseudovirus reporter system enables *in vivo* evaluation of hantavirus entry blockade

To evaluate hantavirus NAbs *in vivo* under Animal Biosafety Level (ABSL)-2 conditions, we generated four luciferase-expressing hantavirus pseudoviruses: rVSV-HTNV-Luc, rVSV-SEOV-Luc, rVSV-SNV-Luc, and rVSV-ANDV-Luc (***Fig. 5a***). After intraperitoneal injection into BALB/c mice, bioluminescence imaging over 9 hours showed that luciferase signals became detectable at 2 hours post-infection, increased progressively from 2 to 6 hours,

and then plateaued between 6 and 9 hours (***Fig. 5b and Extended Data Fig. 6a***). Three-dimensional optical tomography (***Fig. 5c and Extended Data Fig. 6b***) and immunohistochemistry (***Fig. 5d and Extended Data Fig. 6c***) further identified the lungs and intestines as the principal sites of pseudovirus accumulation. These results establish an ABSL-2-compatible *in vivo* reporter platform for tracking hantavirus pseudovirus entry and define a suitable time window for assessing antibody-mediated entry blockade.

To validate this system, pseudoviruses were pre-incubated with antibodies for 1 hour at 37°C before intraperitoneal administration (***Fig. 5e***). At 6 hours post-infection, mice receiving isotype control antibody showed robust bioluminescence, whereas treatment with XA-3H12, XA-044, the XA-3H12/XA-044 cocktail, or IgG-scFv markedly reduced HTNV pseudovirus signals (***Fig. 5f and Extended Data Fig. 7a***). For SEOV pseudovirus, efficient entry blockade was observed with XA-3H12, the cocktail, and IgG-scFv, whereas XA-044 alone showed limited activity (***Fig. 5g and Extended Data Fig. 7a***). Conversely, XA-044, the cocktail, and IgG-scFv potently inhibited SNV and ANDV pseudovirus entry, while XA-3H12 alone was ineffective (***Fig. 5h,i and Extended Data Fig. 7a***). Thus, the in vivo entry-blockade profiles closely matched the in vitro neutralization breadth of each antibody, validating this pseudovirus reporter system as a robust platform for evaluating hantavirus NAbs *in vivo*.

Bispecific strategies confer broad hantavirus entry blockade *in vivo*

To evaluate the prophylactic efficacy of these antibodies *in vivo*, we administered individual mAbs, the XA-044/XA-3H12 cocktail, or the bispecific IgG-scFv intraperitoneally to BALB/c mice 18 hours before challenge with luciferase-expressing hantavirus pseudoviruses. Viral entry was assessed by bioluminescence imaging 6 hours after pseudovirus challenge (***Fig. 6a***). Compared with isotype-control-treated mice, all antibody-treated groups showed markedly reduced HTNV pseudovirus signals, indicating effective blockade of HTNV entry by XA-044, XA-3H12, the cocktail, and IgG-scFv (***Fig. 6b and Extended Data Fig. 7b***). Consistent with their *in vitro* neutralization profiles and the pre-incubation blockade results, XA-044 conferred limited protection against SEOV pseudovirus, whereas XA-3H12 failed to protect against SNV and ANDV pseudoviruses. In contrast, mice pre-treated with either the XA-044/XA-3H12 cocktail or IgG-scFv exhibited markedly reduced luminescence across all

four pseudovirus challenges (***Fig. 6b,e and Extended Data Fig. 7b***). These results demonstrate that both the antibody cocktail and the bispecific IgG-scFv provide broad prophylactic protection against entry of diverse hantavirus pseudoviruses, spanning both OWHs and NWHs.

Post-exposure antibody therapy protects mice from lethal HTNV challenge

We next evaluated the therapeutic efficacy of the XA-044/XA-3H12 cocktail and the bispecific IgG-scFv in a lethal authentic HTNV infection model in suckling mice. Given the clinical relevance of post-exposure intervention, antibodies were administered 24 h after HTNV challenge (***Fig. 6f***). In the isotype-control group, mortality began on day 15, and all animals succumbed to infection by day 18 post-infection. By contrast, both the XA-044/XA-3H12 cocktail and the bispecific IgG-scFv conferred substantial protection, with only 1 and 2 deaths observed in the cocktail- and IgG-scFv-treated groups, respectively (***Fig. 6g***). Consistent with these survival outcomes, isotype-control-treated mice exhibited weight stagnation or loss beginning around day 14 post-infection, whereas antibody-treated mice continued to gain weight throughout the observation period (***Fig. 6g***). Quantification of viral RNA by qRT-PCR at the endpoint further showed that HTNV RNA was undetectable or markedly reduced in the brain, lungs, spleen, and kidneys of antibody-treated mice, indicating that post-exposure antibody administration effectively restricted systemic viral dissemination (***Fig. 6h***). Collectively, these findings demonstrate that both the XA-044/XA-3H12 cocktail and the bispecific IgG-scFv provide potent post-exposure protection against lethal HTNV infection *in vivo*.

DISCUSSION

Hantaviruses remain a persistent and significant zoonotic threat, as illustrated by the recent Andes virus outbreak linked to a South American cruise ship [24]. Their broad rodent reservoirs, recurrent spillover, and—in the case of Andes virus—capacity for human-to-human transmission underscore the need for countermeasures that can protect against diverse hantaviruses, including those that may emerge in future outbreaks. However, no approved specific therapeutics or broadly protective vaccines are currently available. Antibody development has

been constrained by the antigenic diversity of the Gn-Gc glycoprotein complex, with most neutralizing antibodies exhibiting either lineage-restricted activity or limited broad-spectrum potency when targeting a single epitope. In this study, we establish a dual-epitope bispecific strategy to overcome these limitations and broaden hantavirus antibody coverage. By simultaneously engaging two distinct conserved neutralization sites recognized by XA-044 and XA-3H12 within an IgG-scFv architecture, we achieve broad neutralization against representative OWHs and NWHs, conferring robust *in vivo* protection across diverse pseudovirus and lethal HTNV challenge models.

Cryo-EM structures reveal the basis of broad neutralization against both OWHs and NWHs. XA-044 recognizes a conserved epitope at the apical Gn-Gc interface, with key contacts extending into the Gc fusion-loop region [12]. Although this epitope includes a relatively less conserved Gn capping loop, its broader footprint on the highly conserved apical Gc surface likely underlies the breadth of XA-044, and suggests a mechanism of fusion blockade similar to that proposed for ADI-65534 and ADI-42898 [13,21]. XA-3H12, in contrast, binds the basal region of Gc domain II and likely disrupts Gn-Gc lattice assembly on the virion surface. Thus, XA-044 and XA-3H12 define two spatially separated but conserved vulnerabilities on the hantavirus glycoprotein complex.

The structural and functional data support a combinatorial strategy for achieving broad-spectrum hantavirus protection. Although individual antibodies with cross-reactive activity have been described [20,21], the antigenic divergence between OWHs and NWHs makes it difficult for a single specificity to combine maximal potency and breadth. In this context, XA-044 and XA-3H12 provide a rational two-antibody solution. Competition-binding experiments demonstrated that the two antibodies recognize non-overlapping epitopes on the Gn-Gc complex and can bind antigen simultaneously, while neutralization assays showed that their combined use produces synergistic activity. These findings provide a mechanistic rationale for dual targeting: simultaneous engagement of two conserved neutralizing sites can expand broad-spectrum coverage while potentially increasing the genetic barrier to escape. To translate this concept into a single-molecule format, we evaluated five bispecific antibody designs and found that only the IgG-scFv format matched or exceeded the cocktail. A plausible explanation is architectural: the longer and more flexible IgG-scFv format may better

accommodate the distance between the XA-044 and XA-3H12 epitopes, allowing simultaneous engagement on the same virion or neighboring glycoprotein complexes. By contrast, more compact formats, including knob-into-hole, CrossMab, and Fab-scFv, may position the two binding arms too closely or impose geometric constraints that limit productive dual engagement. Importantly, with efficacy comparable to the cocktail in vitro and in vivo, the IgG-scFv format offers practical advantages as a single therapeutic product, including simplified manufacturing, release testing, dosing, and clinical development relative to a two-component cocktail. More broadly, bispecific targeting of two conserved but distinct epitopes may provide a generalizable strategy for developing antibody countermeasures against antigenically diverse bunyaviruses.

A major practical barrier in hantavirus countermeasure development is the restricted access, high cost and low throughput of authentic-virus studies under high-containment conditions. For instance, HTNV and SEOV generally require ABSL-3, whereas highly pathogenic NWHs such as ANDV and SNV require ABSL-4. To address this limitation, we established a ABSL-2-compatible bioluminescent pseudovirus challenge model bearing hantavirus Gn-Gc glycoproteins, enabling rapid and quantitative *in vivo* assessment of neutralizing antibodies across multiple hantaviruses. The concordance between this model and the authentic HTNV lethal challenge—both identifying the cocktail and IgG-scFv as protective and revealing the limitations of individual antibodies—supports its utility as a preclinical prioritization tool. Although this system cannot fully replace authentic-virus protection studies, it can serve as an efficient prescreening step to prioritize candidates before costly and labor-intensive high-containment experiments. This platform should also facilitate evaluation of both passive antibody-based protection and active vaccine-induced neutralizing responses against panels of antigenically diverse hantaviruses.

This study has several limitations. First, although protection against authentic HTNV was demonstrated, live-virus validation against BSL-4-restricted ANDV and SNV remains essential but was beyond the scope of the present study due to containment and strain-access limitations. Second, further studies using serial passage or deep mutational scanning will be needed to define potential escape mutations for both the antibody cocktail and the IgG-scFv bispecific antibody. Third, the *in vivo* pseudovirus model does not capture post-entry steps of

338 viral replication, pathogenesis, or Fc-mediated antibody functions. Finally, the neonatal
339 mouse HTNV challenge model does not fully recapitulate adult immunity or human hanta-
340 virus disease, therefore the 24 h post-exposure efficacy observed in this model has limited
341 clinical relevance; the therapeutic window, optimal dosing, and durability of protection
342 should be further evaluated in more disease-relevant models, such as non-human primates.
343 Nonetheless, the ability of XA-044 and XA-3H12 to simultaneously target two conserved
344 sites of vulnerability on the Gn-Gc complex supports a dual-specificity strategy for both anti-
345 body therapy and rational pan-hantavirus vaccine design.
346
347 **METHODS**
348 **Human subjects and PBMC isolation**
349 Convalescent blood samples were collected from four HFRS donors admitted by Tangdu
350 hospital in 2023-2024. PBMCs and matched plasma samples were obtained from convales-
351 cent patients more than 6 months after discharge. The participants gave written informed con-
352 sent to participate in this study. This study was approved by the Ethics Review Committee of
353 Tangdu Hospital (IEC of Institution for National Drug Clinical Trials, Tangdu Hospital,
354 Fourth Military Medical University, approval # 202409-14 and K202410-35) and Ethics Re-
355 view Committee of Westlake University (approval # 20240423LDP001).
356 Peripheral blood samples were obtained from donors in EDTA-coated collection tubes
357 and processed immediately for PBMC isolation using lymphocyte separation tubes
358 (DAKEWE, Cat # 7922112). Blood samples were centrifuged at 400 × g for 20 min to sepa-
359 rate plasma and cellular components. The plasma fraction was harvested and preserved at
360 −80 °C for subsequent analyses. The remaining blood cells were diluted with an equal volume
361 of D-PBS (Servicebio, Cat # G4200) and subjected to density-gradient centrifugation. Mono-
362 nuclear cells enriched at the interphase were carefully collected and stored at -80 °C until fur-
363 ther use.
364
365 **Recombinant Protein Expression, Purification, and Biotinylation**
366 Codon-optimized sequences encoding the Gn head domain (1,062 bp) and Gc ectodo-
367 main (1,347 bp) consensus sequences of HTNV and SEOV [25]were individually cloned into

the Drosophila S2 expression vector pMT/BiP with a C-terminal Avi-tag and 6×His-tag. The Gn head domain (1,071 bp) and Gc ectodomain (1,341 bp) sequences of SNV[26], and the Gn head domain (1,068 bp) and Gc ectodomain (1,350 bp) sequences of ANDV[27] were individually cloned into the Drosophila S2 expression vector pMT/BiP with a C-terminal 6×His-tag. For the generation of heterodimeric $Gn^{H}Gc$ constructs from HTNV, SEOV, SNV, and ANDV, the Gn head domain and Gc ectodomain were linked by the amino acid sequence GGSGLVPRGSGGGSGGGSWSHPQFEKGGGTGGGTLVPRGSGTGG as previously described[12], and the resulting constructs were individually cloned into pMT/BiP with a C-terminal 6×His-tag. Recombinant plasmids were transfected into Drosophila S2 cells (Invitrogen, Cat # K2780-01), and stable cell lines were generated by selection with blasticidin (25 μg/ml; Beyotime, Cat # ST018). Protein expression was induced with 10 μM $CdCl_2$ (Macklin, Cat # C805627) for 5 days. Culture supernatants were collected, filtered through a 0.22-μm membrane, and buffer-exchanged using a 10-kDa MWCO VIVAFLOW 200 module (Sartorius, Cat # VF20H0) to remove residual $CdCl_2$. Recombinant proteins were purified by Ni^{2+} affinity chromatography (SunResin, Cat # A453201) using an ÄKTA system and subsequently biotinylated through the Avi-tag using a Biotin Labeling Kit (Beyotime, Cat # P0630S).

Isolation and Sorting of Antigen-Specific B Cells

B cells were enriched from PBMCs using a human pan-B cell isolation kit (BioLegend, Cat # 480082) and stained with Zombie Aqua viability dye (BioLegend, Cat # 423102), anti-human CD14-BV605 (BioLegend, Cat # 301834), anti-human CD16-BV785 (BioLegend, Cat # 302046), anti-human CD3-PE-Cy5 (BioLegend, Cat # 300310), anti-human CD19-APC-Cy7 (BioLegend, Cat # 363010), anti-human IgD-FITC (BioLegend, Cat # 348206), and anti-human IgM-PerCP-Cy5.5 (BD Biosciences, Cat # 561285) for 30 min at 4 °C in the dark. To identify HTNV- and SEOV-specific B cells, biotinylated Gn or Gc proteins were precomplexed with PE-streptavidin (BioLegend, Cat # 405204) or APC-streptavidin (BioLegend, Cat # 405207) to generate tetrameric probes, followed by incubation with enriched B cells. Cells were analyzed and sorted on a CytoFLEX SRT flow cytometer (Beckman Coulter). Antigen-specific B cells were defined as $CD14^{-}CD16^{-}CD3^{-}CD19^{+}IgM^{-}IgD^{-}PE^{+}$ or $CD14^{-}CD16^{-}CD3^{-}CD19^{+}IgM^{-}$ $IgD^{-}APC^{+}$ populations.

For antibody gene amplification and cloning, single antigen-specific B cells were sorted into 96-well PCR plates containing 20 μL lysis buffer per well [2.5 μL 10× RT buffer, 2.5 μL 5× gDNA wiper mix (Vazyme, Cat # R312), 0.0625 μL IGEPAL (Sigma-Aldrich, Cat # I8896), 0.5 μL carrier RNA (Sangon Biotech, Cat # B518271-0100), and 14.4375 μL nuclease-free water]. Plates were briefly centrifuged and stored at −80 °C until use. For single-cell transcriptome and BCR sequencing, antigen-specific B cells were sorted into D-PBS containing 2% FBS, counted, and processed for downstream sequencing analyses.

Single B Cell PCR

Single B-cell antibody gene amplification and cloning were performed as previously described [28]. Briefly, cDNA was synthesized from individually sorted B cells using the HiScript III First-Strand cDNA Synthesis Kit (Vazyme, Cat # R312). Immunoglobulin heavy-chain (HC) and light-chain (LC) variable regions were amplified by two rounds of PCR. The first round used primers targeting the 5′ leader and immunoglobulin constant regions to amplify multiple Ig isotypes, followed by nested PCR for specific amplification of HC and LC variable regions and incorporation of homologous sequences compatible with expression vectors. PCR products were analyzed on 1% agarose gels, and fragments of approximately 500 bp (HC) and 450 bp (LC) were purified, linearized, and used for small-scale antibody expression.

Single-cell BCR sequencing and antibody gene screening

Antigen-specific memory B cells were sorted and loaded onto a Chromium Next GEM Chip (10x Genomics). Single-cell capture, lysis, and first-strand cDNA synthesis were performed using the Chromium Single Cell 5′ Library & Gel Bead Kit (10x Genomics) according to the manufacturer's instructions. Gene expression and V(D)J libraries were generated using the Chromium Single Cell V(D)J Reagent Kits (10x Genomics). Libraries were sequenced on an Illumina NovaSeq X Plus platform in paired-end 150-bp mode.

Single-cell BCR sequencing data were assembled and initially annotated using the V(D)J module of Cell Ranger (v7.2), with the GRCh38 Human V(D)J reference dataset (GRCh38-alts-ensembl-7.1.0) downloaded from 10x Genomics. Among a total of 1,959 cells, 1,894 cells contained productive V-J spanning pairs. Antibody clonal lineage identification was

performed using an optimized Change-O workflow. Human IG reference sequences from the IMGT database were used for IgBLAST annotation and germline reconstruction, while Cell Ranger V(D)J annotation results were additionally incorporated for single-cell BCR datasets.

To determine the clonal clustering threshold, nearest-neighbor distances between productive BCR heavy-chain sequences were calculated using the `distToNearest` function in the shazam package. Junction nucleotide sequences sharing identical V- and J-gene assignments were compared using normalized Hamming distances. The resulting nearest-neighbor distance distribution typically exhibits a bimodal pattern, representing intra-clonal diversification driven by SHM and inter-clonal sequence diversity, respectively. A Gaussian mixture model (GMM) was fitted to the nearest-neighbor distance distribution using the `findThreshold` function with the `gmm` method. The threshold separating clonally related and unrelated sequences was defined as the intersection between the two inferred Gaussian components. This threshold (0.285103) was subsequently used for clone assignment in downstream repertoire analyses.

Candidate antibodies for downstream characterization were selected from all identified BCR repertoires according to the following criteria: (i) complete paired heavy- and light-chain sequences detected within the same single cell; (ii) SHM rate greater than 3%; (iii) heavy-chain CDRH3 length greater than 17 amino acids; and (iv) light-chain CDRL3 length greater than 8 amino acids.

Expression and purification of mAbs

For antibodies derived from single B-cell PCR, purified PCR products were assembled into linear human IgG expression cassettes by overlapping PCR as previously described2. For antibodies identified by single-cell BCR sequencing, heavy- and light-chain variable genes were synthesized and cloned into mammalian expression vectors. Expression cassettes or plasmids were transiently transfected into Expi293F cells using PEI MAX (Polysciences). Culture supernatants containing recombinant IgGs were harvested for antibody quantification and preliminary ELISA screening. For pseudovirus neutralization assays, antibody plasmids were transfected into 15 mL Expi293F cultures, and antibodies were harvested after 5 days and purified using protein A magnetic beads (GenScript, Cat # L00695).

For large-scale antibody production, heavy- and light-chain plasmids were co-transfected into Expi293F cells at a 1:1.5 ratio using PEI MAX. Supernatants were collected 5 days post-transfection, clarified by centrifugation, filtered through a 0.22-μm membrane, and purified by protein A affinity chromatography (SunResin, Cat # A4093101) on an ÄKTA system. Bound antibodies were eluted with 100 mM glycine (pH 2.5), immediately neutralized with 1/10 volume of 1 M Tris-HCl, and buffer-exchanged into PBS.

ELISA

For preliminary screening, 96-well high-binding ELISA plates were coated overnight at 4 °C with glycoproteins (1 μg/mL). Plates were washed three times with PBST (0.1% Tween-20 in D-PBS) and blocked with 3% BSA in PBST for 2 h at 37 °C. Recombinant IgG-containing supernatants (100 μL/well) were added and incubated for 2 h at 37 °C. After five washes, plates were incubated with HRP-conjugated anti-human IgG antibody (Promega, Cat # W4031; 1:5,000 dilution) for 1 h at 37 °C. Plates were washed five times, developed with TMB substrate (Beyotime, Cat # P0209) for 10 min at room temperature in the dark, and the reaction was terminated with 50 μL of 1 M sulfuric acid. Absorbance was measured at 450 nm.

For quantitative binding analysis, purified antibodies were serially diluted 3-fold from an initial concentration of 10 μg/mL and added to antigen-coated plates prepared as described above. Incubation, washing, and detection procedures were performed under identical conditions. All assays were performed in duplicate.

Generation of pseudotyped VSVs

All pseudotyped viruses were generated using pLVX plasmids encoding the M segment of HTNV[29], SEOV[30], SNV[26], ANDV[27], LNV[31], or JUQV[32]. HEK293T cells were seeded in 10-cm dishes and transfected 12 h later with M-segment expression plasmids (12 μg), psPAX2 (9 μg), and pMD2.G (3 μg) using PEI MAX. At 12 h post-transfection, the medium was replaced with fresh culture medium. Lentivirus-containing supernatants were harvested 48 h later and stored at −80 °C. Stable HEK293T cell lines expressing HTNV M, SEOV M, SNV M, ANDV M, LNV M, or JUQV M were generated by lentiviral transduction followed

by puromycin selection.

For rVSV production, all pseudotyped viruses were produced according to previously described protocols [33]. Stable M-expressing HEK293T cells were seeded in 10-cm dishes and infected 12 h later with rVSV-GFP or rVSV-luc for 1 h at 37 °C. Cells were washed five times with PBS and maintained in Opti-MEM containing 2% FBS. Supernatants containing rVSV-HTNV, rVSV-SEOV, rVSV-SNV, rVSV-ANDV, rVSV-LNV, or rVSV-JUQV were collected 24-36 h post-infection, clarified by centrifugation, filtered through a 0.45-μm membrane, and stored at −80 °C until use.

Pseudovirus neutralization assay

Neutralization activity was evaluated using rVSV-based hantavirus pseudoviruses expressing GFP, including rVSV-HTNV, rVSV-SEOV, rVSV-SNV, rVSV-ANDV, rVSV-LNV, and rVSV-JUQV. Vero cells were seeded in 96-well plates at 5×10^3 cells per well one day before infection. Antibodies were subjected to 3-fold serial dilution in complete medium and pre-incubated with pseudoviruses for 1 h at 37 °C. The antibody-virus mixtures were subsequently transferred onto Vero cells and incubated for an additional 1 h at 37 °C to facilitate viral entry. Following incubation, cells were washed to remove unbound virus, and fresh complete medium was added. Infection was assessed 24 h later by detection of GFP-positive cells using fluorescence microscopy or an Operetta CLS high-content imaging system (Perkin Elmer, HTCF-AW004). IC_{50} values were determined by fitting dose-response curves with a four-parameter nonlinear regression model in GraphPad Prism 10.

Authentic virus neutralization assay

Neutralizing activity against authentic HTNV (strain 76118) was evaluated in Vero E6 cells using an immunofluorescence-based assay. Monoclonal antibodies were serially diluted 2-fold in complete culture medium and incubated with HTNV at the indicated dose (100 $TCID_{50}$ per well) for 1 h at 37 °C. The antibody and virus mixtures were subsequently transferred to Vero cells seeded in 96-well plates and incubated at 37 °C for 1 h to facilitate viral entry. After incubation, remove unbound viruses by washing, replenish with fresh complete medium and incubate for another 72 hours. Following infection, culture supernatants were

removed, and cells were fixed and permeabilized with pre-chilled 80% acetone for 30 min at room temperature. Plates were washed twice with PBST and incubated with HTNV-NP-mAb [34] for 2 h at 37 °C. After washing, cells were stained with Alexa Fluor 488-conjugated goat anti-mouse IgG secondary antibody (Proteintech, Cat# SA00013-1; 1:400 dilution) for 1 h at 37 °C in the dark, followed by nuclear counterstaining with DAPI (Proteintech, Cat# PR30021) for 15 min. Fluorescent signals were visualized using a fluorescence microscope. Neutralization potency was quantified by calculating IC_{50} values using a four-parameter non-linear regression model in GraphPad Prism 10.

BLI

Cross-competition and binding kinetics were characterized at 30 °C using an Octet R8 system (Sartorius). For epitope binning, HTNV $Gn^{H}Gc$ was immobilized onto HIS1K biosensors (Sartorius) in assay buffer (D-PBS + 0.1% BSA). Following saturation with a primary mAb, the sensors were exposed to a secondary mAb to monitor competitive binding. Data were processed using the Epitope Binning module in Octet Analysis Studio, with signal shifts recorded as relative light units (RLU).

For kinetic profiling, $Gn^{H}Gc$ -loaded sensors underwent a 120-s baseline equilibration before immersion in serial three-fold dilutions of mAbs. Association and dissociation were monitored for 300 s and 1,000 s, respectively. Sensors were regenerated with Glycine-HCl (pH 1.7) between cycles. Binding kinetics were fitted using a 1:1 Langmuir binding model in Octet Analysis Studio v13.0.2.46.

Flow cytometry binding assay

To evaluate antibody binding to different hantavirus glycoproteins, stable HEK293T cell lines expressing individual M-segment proteins were generated, including HTNV[29], SEOV[30], SNV[26], ANDV[27], LNV[31], JUQV[32], PUUV[35], DOBV[36], and CHOV (YP_009506070.1). Briefly, 1×10^6 cells were collected, washed, and resuspended in 100 µL PBS. Cells were incubated with 10 µg primary antibodies for 1 h on ice, followed by three washes with PBS to remove unbound antibodies. Bound antibodies were detected using a PE anti-human IgG Fc Antibody (Beyotime, Cat#410708) incubated for 1 h on ice in the dark. After three additional

washes, cells were resuspended in PBS and analyzed on a Cytek Aurora spectral flow cytometer. Data were processed using FlowJo software, and antibody binding was quantified as median fluorescence intensity (MFI).

In vivo evaluation of mAb efficacy using rVSV pseudoviruses

Luciferase-expressing pseudoviruses, including rVSV-HTNV, rVSV-SEOV, rVSV-SNV, and rVSV-ANDV, were generated as described above. Female BALB/c mice (6 weeks old) were inoculated intraperitoneally (i.p.) with the indicated pseudoviruses. At designated time points post-inoculation, mice were anesthetized by intraperitoneal administration of 1% pentobarbital sodium and subsequently injected i.p. with D-luciferin (1.5 mg per mouse; Beyotime, Cat # ST198). Bioluminescence signals were acquired using a Lumina III in vivo imaging system (Revvity), and three-dimensional optical tomographic reconstruction was performed using the IVIS Spectrum imaging system (PerkinElmer).

For antibody pre-incubation assays, pseudoviruses were incubated with monoclonal antibodies (6.25 mg/kg) at 37 °C for 1 h before i.p. administration into BALB/c mice. Bioluminescence imaging was performed 6 h post-inoculation as described above. For prophylactic protection experiments, monoclonal antibodies (6.25 mg/kg) were administered i.p. 18 h before pseudovirus challenge, followed by in vivo imaging analysis 6 h after infection. The pseudoviruses challenge works were conducted in an ABSL-2 facility, where mice were provided with adequate food and water throughout the experiment. Ethical approval for the animal challenge study was obtained from the Biosafety Committee of Westlake University (Approval ID: AP # 25-164-LDP).

In vivo evaluation of mAb efficacy using authentic virus

The therapeutic efficacy of the antibody cocktail and IgG-scFv construct was evaluated in neonatal BALB/c mice. Mice were challenged intraperitoneally with authentic HTNV (strain 76118) at a dose of 5×10^5 PFU in 30 μL per mouse. At 24 h post-infection, mice received intraperitoneal administration of either the antibody cocktail (6.25 mg/kg), IgG-scFv (6.25 mg/kg), or an isotype-matched human control antibody (6.25 mg/kg). Survival and body weight were monitored for 25 days. To assess viral burden and tissue distribution, brain

samples were collected at the endpoint for quantitative PCR analysis. All the authentic HTNV works were conducted in the ABSL-3 facility at Wuhan University, where mice were provided with adequate food and water throughout the experiment. Ethical approval for the animal challenge study was obtained from the Biosafety Committee of Wuhan University (Approval ID: AP # WQ20210048).

Immunofluorescence

Tissues were fixed overnight at 4 °C in 4% paraformaldehyde, cryoprotected in 30% sucrose for 48 h, and embedded in OCT compound. Cryosections (10 μm thickness) were prepared for immunofluorescence analysis. Sections were fixed with 4% paraformaldehyde for 10 min at room temperature, washed three times with PBS, and permeabilized with 0.25% Triton X-100. After additional PBS washes, sections were blocked with 5% rat serum at room temperature. Primary staining was performed for 1 h at room temperature using either anti-GFP antibody (Abclonal, Cat # AE012; 1:100 dilution) or ascitic fluid from HTNV-Gn-immunized mice (1:5,000 dilution). Following three washes with PBS, sections were incubated with Alexa Fluor 488-conjugated goat anti-mouse IgG (H+L) secondary antibody (Invitrogen, Cat # A-11029; 1:2000 dilution) for 1 h at room temperature. Sections were then washed, mounted with DAPI-containing antifade mounting medium (Beyotime, Cat # P0131), and imaged using a Zeiss LSM 900 inverted confocal microscope (Zeiss, WLL-W-20220039).

Viral RNA extraction and quantification

HTNV viral RNA was quantified by quantitative polymerase chain reaction (qPCR). Total RNA was extracted from trizol homogenates (TaKaRa, Cat#9109) of brain tissues using the high-throughput automatic nucleic acid extraction system (Thermo Fisher Scientific, KingFisher Flex). Tissue weights were recorded before homogenization to enable normalization. Viral RNA levels were quantified by two-step RT–qPCR. Reverse transcription was performed using Hifair III SuperMix Plus (Yeasen, Cat# H7514240), followed by quantitative PCR using Hieff qPCR SYBR Green Master Mix (Yeasen, Cat#WH2518011). The HTNV NP segment was amplified using the following primers and probe: forward primer, 5′-CAG TGC TAC CCT GCA AAG AA-3′; reverse primer, 5′-ATT GTT CGA TAC GAT CAC TCC-3′; and

probe, 5′-FAM/TCA TCC TCC TTG GAT ATG CAG GCC TCA/BHQ1-3′. Reactions were carried out on an Archimed R4 Real-Time PCR Detection System (ROCGENE) in a total volume of 20 μL containing 1 μL each of forward primer, reverse primer, and probe, 5 μL RT–PCR enzyme mix, 5 μL RNA template, and 7 μL nuclease-free water. Thermal cycling conditions consisted of reverse transcription at 50 °C for 15 min, initial denaturation at 95 °C for 2 min, followed by 40 cycles of 95 °C for 5 s and 60 °C for 31 s, with fluorescence acquisition at each extension step. Relative viral RNA levels were determined by comparative quantification using the mean Ct values of the HTNV NP gene normalized to those of the housekeeping gene GAPDH. Relative expression levels were calculated using the $2^{-\Delta\Delta Ct}$ method.

Cryo-EM sample preparation and data collection

For the hantavirus $Gn^{H}Gc$-Fab complexes, purified $Gn^{H}Gc$ protein was mixed with XA-044 or XA-3H12 at a molar ratio of 1:3 and incubated at 37°C for 1 h before loading onto a Superose 200 Increase 10/300 column (GE Healthcare, 29091596) equilibrated in buffer containing 50 mM Tris and 150 mM NaCl, pH 7.4. Fractions containing the complex were concentrated using a 50-kDa molecular weight cut-off concentrator (Amicon Ultra UFC510096). Protein quality was assessed by preparative size-exclusion chromatography (Inscinstech Unique Autopre), SDS-PAGE and western blotting.

A 5 μL aliquot of 0.1 mg/mL $Gn^{H}Gc$-Fab complex was applied to freshly glow-discharged holy carbon grids (Quantifoil R2/2, Cu 200 mesh; 30 s at 20 mA) and plunge-frozen using a Vitrobot Mark IV (Thermo Fisher Scientific) with a blot force of 0, blot time of 2 s, 80% humidity and 4°C. Data were collected using EPU software (Thermo Fisher Scientific) to control an FEI Titan Krios G4 transmission electron microscope operated at 300 kV and equipped with a Falcon 4i Summit direct electron detector and a Selectris X energy filter. Automated data collection was performed at a nominal magnification of 130,000×, corresponding to a pixel size of 0.97 Å. The dose rate was set to 7.78 counts per physical pixel per second. In total, 14,202 movies of the SNV $Gn^{H}Gc$-XA-044 complex and 16,555 movies of the HTNV $Gn^{H}Gc$-XA-3H12 complex were collected, with defocus values ranging from 0.9 to 1.8 μm.

Cryo-EM model building and analysis

UCSF ChimeraX and Coot were used to fit atomic models into the density maps, including XA-044 heavy chain (PDB 7S0B), XA-044 light chain (PDB 7CZU), XA-3H12 heavy chain (PDB 7CZQ), XA-3H12 light chain (PDB 8R9Y), HTNV Gn (PDB 6Y6P), HTNV Gc (PDB 5LJY), SNV Gn (PDB 8AHN) and SNV Gc (PDB 6Y5W) [37,38]. The full complex and Gn^{H}Gc-Fab regions were then manually rebuilt in Coot [37]. The models were refined using Rosetta [39]. Figures were generated using UCSF ChimeraX [38]. Protein-protein interactions have been analyzed by PISA [40].

Quantification and Statistical Analysis

GraphPad Prism 10 software was used for data visualization and statistical analyses. Statistical comparisons between two groups were performed using unpaired, two-tailed Mann-Whitney test. Data are presented as mean ± SEM unless otherwise indicated. Statistical significance was defined as ns (not significant, $p \geq 0.05$), * $p < 0.05$, ** $p < 0.01$, *** $p < 0.001$, and **** $p < 0.0001$.

ACKNOWLEDGMENTS

We thank the technical support from the Biomedical Research Core Facility, Laboratory Animal Resources Center, Cryo-EM Facility and High-Performance Computing Center at Westlake University. We thank Chi Biotech Co., Ltd. for assisting in the single-cell sequencing. This work was supported by Westlake Education Foundation (to D.L. and Z.W.), Zhejiang Provincial Key Laboratory Construction Project (2024ZY01026), the National Natural Science Foundation of China (82471858 to D.L. and 82272330 to X.W.), Zhejiang Provincial Natural Science Foundation of China (LR26C080001 to D.L.), the National Key R and D Program of China (2023YFC2605504 to W.H. and 2024YFA1306600 to Z.W.), the Science and Technology Program of Science, Technology and Innovation Commission of Shenzhen Municipality (JCYJ20230807090209018 to W.H.), the Shaanxi Provincial Natural Science Basic Research Program Key Project (2024JC-ZDXM-42 to R.L. and 2025JC-YBMS-988 to Z.L.), and the Assistance Program of Xijing Hospital (XJZT26JS05 to R.L.).

DATA AVAILABILITY

The data and codes that support the findings of this study are available from the corresponding authors on request.

AUTHOR CONTRIBUTIONS

J.Y., Z.J., Y.K., and Z.L. performed experiments. Z.D. performed computational analysis. X.Z., X.D., and J.L. collected human specimens and provided clinical support. Y.K. and Z.W. performed structural studies and analysis. Z.L., X.W., and R.L. conducted and supervised authentic virus *in vitro* studies. Z.J., S.C., L.N., F.L, and W.H. performed and supervised the authentic virus *in vivo* study. J.B., M.L., J.S., Z.Z., F.Y., R.S. and Z.K. provided critical scientific guidance. D.L. conceived, designed, and supervised the study. J.Y., Z.W. and D.L. wrote the paper. All authors reviewed and approved the manuscript.

DECLARATION OF INTERESTS

D.L., J.Y., R.L., Z.L., X.Z., X.W., J.L., X.D. have applied for patents concerning HTNV antibodies that are related to this work. All other authors declare no conflict of interest.

REFERENCES

1 Kuhn, J. H. & Schmaljohn, C. S. A Brief History of Bunyaviral Family Hantaviridae. *Diseases* **11**, doi:10.3390/diseases11010038 (2023).

2 Kruger, D. H., Figueiredo, L. T., Song, J. W. & Klempa, B. Hantaviruses--globally emerging pathogens. *J Clin Virol* **64**, 128-136, doi:10.1016/j.jcv.2014.08.033 (2015).

3 Engdahl, T. B. *et al.* Broad and potently neutralizing monoclonal antibodies isolated from human survivors of New World hantavirus infection. *Cell Rep* **35**, 109086, doi:10.1016/j.celrep.2021.109086 (2021).

4 Jonsson, C. B., Figueiredo, L. T. & Vapalahti, O. A global perspective on hantavirus ecology, epidemiology, and disease. *Clin Microbiol Rev* **23**, 412-441, doi:10.1128/CMR.00062-09 (2010).

5 Vapalahti, O. *et al.* Hantavirus infections in Europe. *Lancet Infect Dis* **3**, 653-661, doi:10.1016/s1473-3099(03)00774-6 (2003).

6 Vial, P. A. *et al.* Hantavirus in humans: a review of clinical aspects and management. *Lancet Infect Dis* **23**, e371-e382, doi:10.1016/S1473-3099(23)00128-7 (2023).

7 Figueiredo, L. T., Souza, W. M., Ferres, M. & Enria, D. A. Hantaviruses and cardiopulmonary syndrome in South America. *Virus Res* **187**, 43-54, doi:10.1016/j.virusres.2014.01.015 (2014).

8 Watson, D. C. *et al.* Epidemiology of Hantavirus infections in humans: a comprehensive, global overview. *Crit Rev Microbiol* **40**, 261-272, doi:10.3109/1040841X.2013.783555 (2014).

9 Avsic-Zupanc, T., Saksida, A. & Korva, M. Hantavirus infections. *Clin Microbiol Infect* **21S**, e6-e16, doi:10.1111/1469-0691.12291 (2019).

10 Afzal, S. *et al.* Hantavirus: an overview and advancements in therapeutic approaches for infection. *Front Microbiol* **14**, 1233433, doi:10.3389/fmicb.2023.1233433 (2023).

11 Plyusnin, A., Vapalahti, O. & Vaheri, A. Hantaviruses: genome structure, expression and evolution *The Journal of general virology* **77 (Pt 11)** (1996).

12 Serris, A. *et al.* The Hantavirus Surface Glycoprotein Lattice and Its Fusion Control Mechanism. *Cell* **183**, 442-456 e416, doi:10.1016/j.cell.2020.08.023 (2020).

13 Guo, L. *et al.* High-resolution in situ structures of hantavirus glycoprotein tetramers. *Cell* **189**, 2731-2747 e2715, doi:10.1016/j.cell.2026.01.030 (2026).

14 Rissanen, I. *et al.* Structural Transitions of the Conserved and Metastable Hantaviral Glycoprotein Envelope. *J Virol* **91**, doi:10.1128/JVI.00378-17 (2017).

15 Guardado-Calvo, P. *et al.* Mechanistic Insight into Bunyavirus-Induced Membrane Fusion from Structure-Function Analyses of the Hantavirus Envelope Glycoprotein Gc. *PLoS Pathog* **12**, e1005813, doi:10.1371/journal.ppat.1005813 (2016).

16 Willensky, S. *et al.* Crystal Structure of Glycoprotein C from a Hantavirus in the Post-fusion Conformation. *PLoS Pathog* **12**, e1005948, doi:10.1371/journal.ppat.1005948 (2016).

17 Heiskanen, T. *et al.* Phage-displayed peptides mimicking the discontinuous neutralization sites of puumala Hantavirus envelope glycoproteins. *Virology* **262**, 321-332, doi:10.1006/viro.1999.9930 (1999).

18 Stass, R. *et al.* Mechanistic basis for potent neutralization of Sin Nombre hantavirus by

a human monoclonal antibody. *Nat Microbiol* **8**, 1293-1303, doi:10.1038/s41564-023-01413-y (2023).

19 Levanov, L., Iheozor-Ejiofor, R. P., Lundkvist, A., Vapalahti, O. & Plyusnin, A. Defining of MAbs-neutralizing sites on the surface glycoproteins Gn and Gc of a hantavirus using vesicular stomatitis virus pseudotypes and site-directed mutagenesis. *J Gen Virol* **100**, 145-155, doi:10.1099/jgv.0.001202 (2019).

20 Mittler, E. *et al.* Human antibody recognizing a quaternary epitope in the Puumala virus glycoprotein provides broad protection against orthohantaviruses. *Sci Transl Med* **14**, eabl5399, doi:10.1126/scitranslmed.abl5399 (2022).

21 Mittler, E. *et al.* Structural and mechanistic basis of neutralization by a pan-hantavirus protective antibody. *Sci Transl Med* **15**, eadg1855, doi:10.1126/scitranslmed.adg1855 (2023).

22 Higa, M. M., Petersen, J., Hooper, J. & Doms, R. W. Efficient production of Hantaan and Puumala pseudovirions for viral tropism and neutralization studies. *Virology* **423**, 134-142, doi:10.1016/j.virol.2011.08.012 (2012).

23 Ray, N., Whidby, J., Stewart, S., Hooper, J. W. & Bertolotti-Ciarlet, A. Study of Andes virus entry and neutralization using a pseudovirion system. *J Virol Methods* **163**, 416-423, doi:10.1016/j.jviromet.2009.11.004 (2010).

24 Basu, M. & Fieldhouse, R. Hantavirus outbreak exposes uncertainty about how disease spreads. *Nature*, doi:10.1038/d41586-026-01512-w (2026).

25 Liu, R. R. *et al.* Investigation of a subunit protein vaccine for HFRS based on a consensus sequence between envelope glycoproteins of HTNV and SEOV. *Virus Research* **334**, doi:10.1016/j.virusres.2023.199149 (2023).

26 Arikawa, J., Lapenotiere, H. F., Iacono-Connors, L., Wang, M. L. & Schmaljohn, C. S. Coding properties of the S and the M genome segments of Sapporo rat virus: comparison to other causative agents of hemorrhagic fever with renal syndrome. *Virology* **176**, 114-125, doi:10.1016/0042-6822(90)90236-k (1990).

27 Meissner, J. D., Rowe, J. E., Borucki, M. K. & St Jeor, S. C. Complete nucleotide sequence of a Chilean hantavirus. *Virus Res* **89**, 131-143, doi:10.1016/s0168-1702(02)00129-6 (2002).

28 Li, D. *et al.* In vitro and in vivo functions of SARS-CoV-2 infection-enhancing and neutralizing antibodies. *Cell* **184**, 4203-+, doi:10.1016/j.cell.2021.06.021 (2021).

29 Schmaljohn, C. S., Schmaljohn, A. L. & Dalrymple, J. M. Hantaan virus M RNA: coding strategy, nucleotide sequence, and gene order. *Virology* **157**, 31-39, doi:10.1016/0042-6822(87)90310-2 (1987).

30 Spiropoulou, C. F. *et al.* Genome structure and variability of a virus causing hantavirus pulmonary syndrome. *Virology* **200**, 715-723, doi:10.1006/viro.1994.1235 (1994).

31 Johnson, A. M. *et al.* Laguna Negra virus associated with HPS in western Paraguay and Bolivia. *Virology* **238**, 115-127, doi:10.1006/viro.1997.8840 (1997).

32 Spruill-Harrell, B. *et al.* Purifying selection constrains the evolution of Juquitiba virus in wild Oligoryzomys nigripes communities. *PLoS Pathog* **22**, e1013839, doi:10.1371/journal.ppat.1013839 (2026).

33 Whitt, M. A. Generation of VSV pseudotypes using recombinant DeltaG-VSV for studies on virus entry, identification of entry inhibitors, and immune responses to vaccines. *J Virol Methods* **169**, 365-374, doi:10.1016/j.jviromet.2010.08.006 (2010).

34 Liu, R. *et al.* HTNV infection of CD8(+) T cells is associated with disease progression in HFRS patients. *Commun Biol* **4**, 652, doi:10.1038/s42003-021-02182-2 (2021).

35 Vapalahti, O., Kallio-Kokko, H., Salonen, E. M., Brummer-Korvenkontio, M. & Vaheri, A. Cloning and sequencing of Puumala virus Sotkamo strain S and M RNA segments: evidence for strain variation in hantaviruses and expression of the nucleocapsid protein. *J Gen Virol* **73 (Pt 4)**, 829-838, doi:10.1099/0022-1317-73-4-829 (1992).

36 Nemirov, K. *et al.* Genetic characterization of new Dobrava hantavirus isolate from Greece. *J Med Virol* **69**, 408-416, doi:10.1002/jmv.10304 (2003).

37 Emsley, P., Lohkamp, B., Scott, W. G. & Cowtan, K. Features and development of Coot. *Acta Crystallogr D Biol Crystallogr* **66**, 486-501, doi:10.1107/S0907444910007493 (2010).

38 Pettersen, E. F. *et al.* UCSF ChimeraX: Structure visualization for researchers, educators, and developers. *Protein Sci* **30**, 70-82, doi:10.1002/pro.3943 (2021).

39 Wang, R. Y. *et al.* Automated structure refinement of macromolecular assemblies from cryo-EM maps using Rosetta. *Elife* **5**, doi:10.7554/eLife.17219 (2016).

40 Krissinel, E. & Henrick, K. Inference of macromolecular assemblies from crystalline state. *J Mol Biol* **372**, 774-797, doi:10.1016/j.jmb.2007.05.022 (2007).

FIGURES AND FIGURE LEGENDS

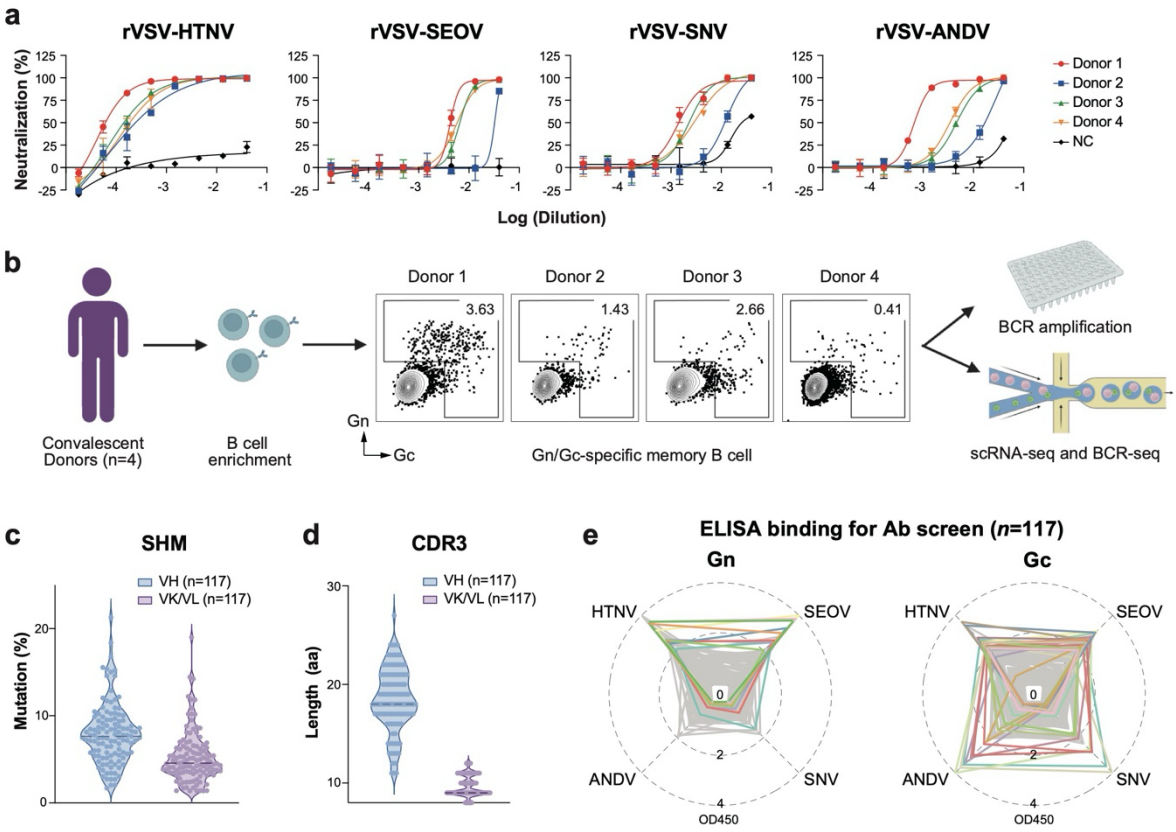

Fig. 1 | Isolation of cross-reactive antibodies from HFRS convalescent patients.

a, Plasma neutralization of GFP-encoding pseudotyped rVSV bearing HTNV, SEOV, SNV, or ANDV glycoproteins. Plasma samples were collected from four convalescent HFRS donors and a healthy donor as the negative control (NC). Percent neutralization was plotted against $\log_{10}$-transformed plasma dilution, and relative infectivity was quantified by GFP-positive cells. Data represent mean ± SEM from two independent replicates.

b, Workflow for antigen-specific memory B cell isolation. B cells were enriched by negative selection, and HTNV- or SEOV-Gn/Gc-specific $IgM^{-}IgD^{-}$ B cells were sorted by FACS for single-cell PCR and BCR sequencing.

c,d, Somatic hypermutation (SHM) frequencies **(c)** and CDR3 length distributions **(d)** in V_H and V_κ/V_λ genes of Gn/Gc-specific BCRs obtained by single-cell PCR (*n*=49) or single-cell BCR sequencing (*n*=68).

e, ELISA-based screening of antibody binding breadth. Radar plots show antibody reactivity to Gn (left panel) and Gc (right panel) of HTNV, SEOV, SNV, and ANDV, with concentric rings indicating OD_{450} values.

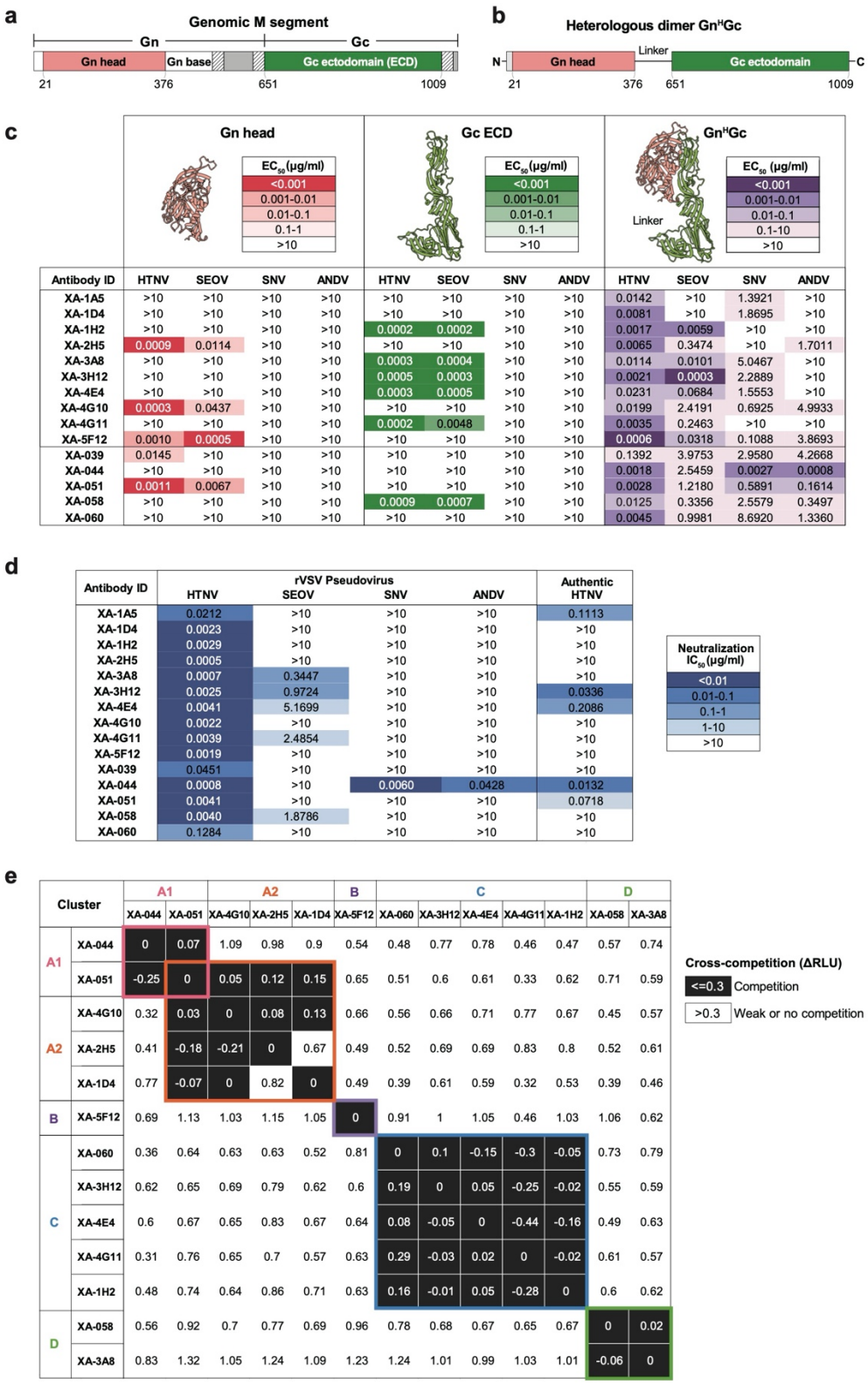

Fig. 2 | Identification of NAbs targeting distinct hantavirus Gn/Gc neutralization sites.

a, Scheme of the hantavirus M segment domain organization, with individual protein domains indicate color-coded.

b, Scheme of the single-chain hantavirus glycoprotein heterodimer $Gn^{H}Gc$ construct.

c, Binding profiles of the downselected neutralizing antibodies. Recombinant Gn head, Gc ectodomain (ECD), and $Gn^{H}Gc$ proteins from HTNV, SEOV, SNV, and ANDV were analyzed by ELISA. Color intensity denotes binding EC_{50}. Data represent mean ± SEM from two independent experiments.

d, Neutralization potency against pseudotyped rVSVs of HTNV, SEOV, SNV, and ANDV, as well as authentic HTNV. Color intensity denotes IC_{50} neutralization titers. Data represent mean ± SEM from two independent experiments.

e, Epitope binning by BLI-based competition analysis. HTNV $Gn^{H}Gc$ antigen was captured by a primary antibody (y axis), followed by binding of a secondary antibody (x axis). Secondary-antibody responses were normalized to maximal uncompeted binding. Antibody pairs were classified as competing (black, ≤ 0.3) or weakly/non-competing (white, >0.3), and grouped by cross-competition profiles.

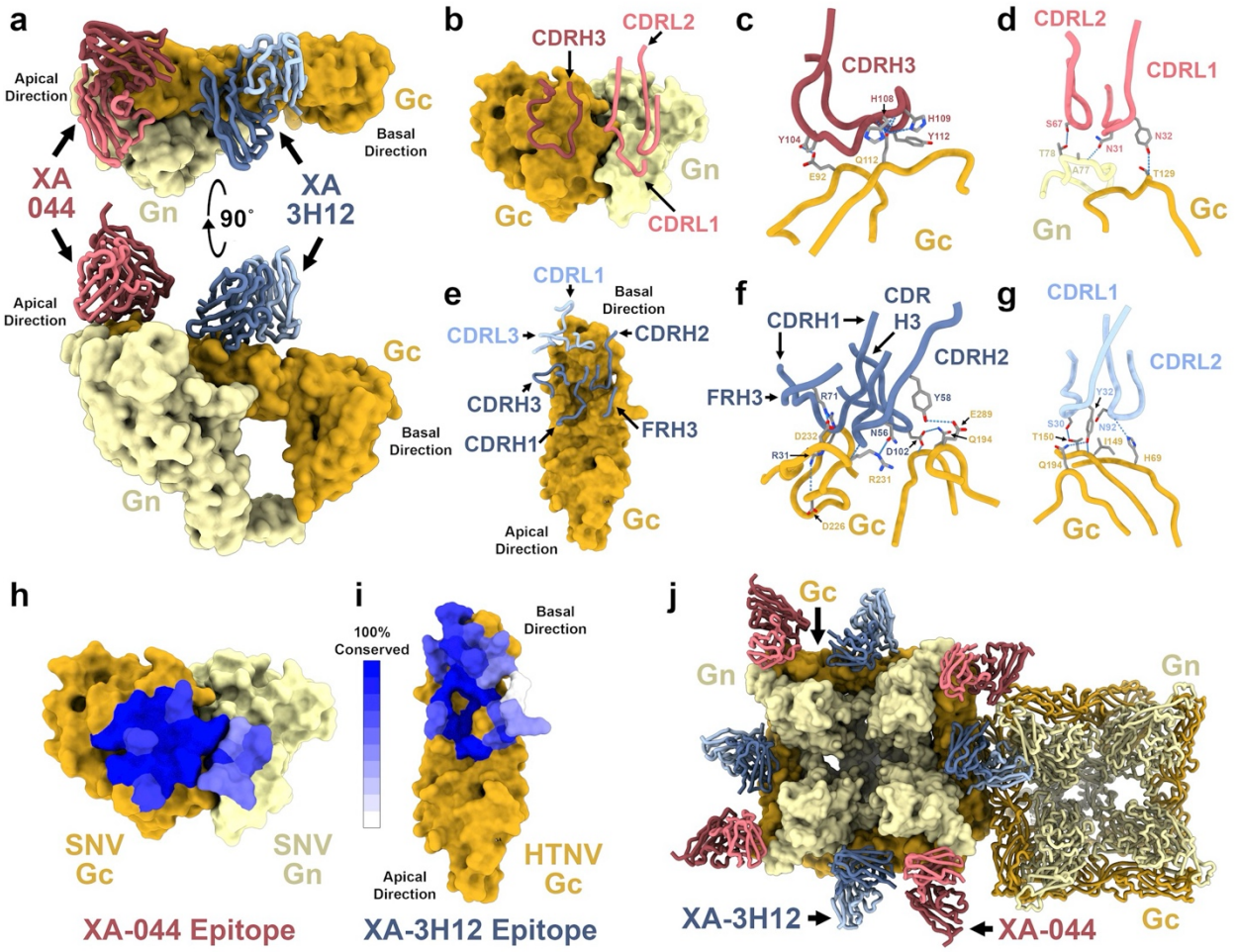

Fig. 3 | Cryo-EM structure of the two distinct neutralization epitopes.

a, XA-044 and XA-3H12 superposed onto the ANDV Gn-Gc dimer (PDB: 9P3Y), showing epitope locations. Fabs are shown as ribbons and Gn-Gc as surface; Gn, yellow; Gc, gold; XA-044 heavy/light chains, dark/light red; XA-3H12 heavy/light chains, dark/light blue.

b, Focused view of XA-044 CDRH/CDRL binding at the SNV Gn-Gc apical interface.

c,d, Zoomed-in views of the SNV Gn-Gc interface with the XA-044 heavy (**c**) or light (**d**) chain, with selected side chains shown as sticks. Hydrogen bonds and salt bridges are shown as cyan dashed lines.

e, Focused view of XA-3H12 CDRH/CDRL binding to the basal region of HTNV Gc domain II.

f,g, Zoomed-in views of the HTNV Gc interface with the XA-3H12 heavy (**f**) or light (**g**) chain, annotated as in (**c**) and (**d**).

h,i, Molecular surface of XA-044 (**h**) and XA-3H12 (**i**) epitopes on SNV Gn-Gc and HTNV Gc, respectively, colored by hantavirus residue conservation using a 10-step Clustal Omega gradient from deep blue to white, corresponding to scores of 100 to 0.

j, XA-044 and XA-3H12 super-positioned onto ANDV Gn-Gc tetramer with neighboring tetramer (PDB

ID: 9P3Y and 9P3X), where main tetramer rendered in surface and neighboring tetramer in ribbon. Color scheme is the same as in (**a**).

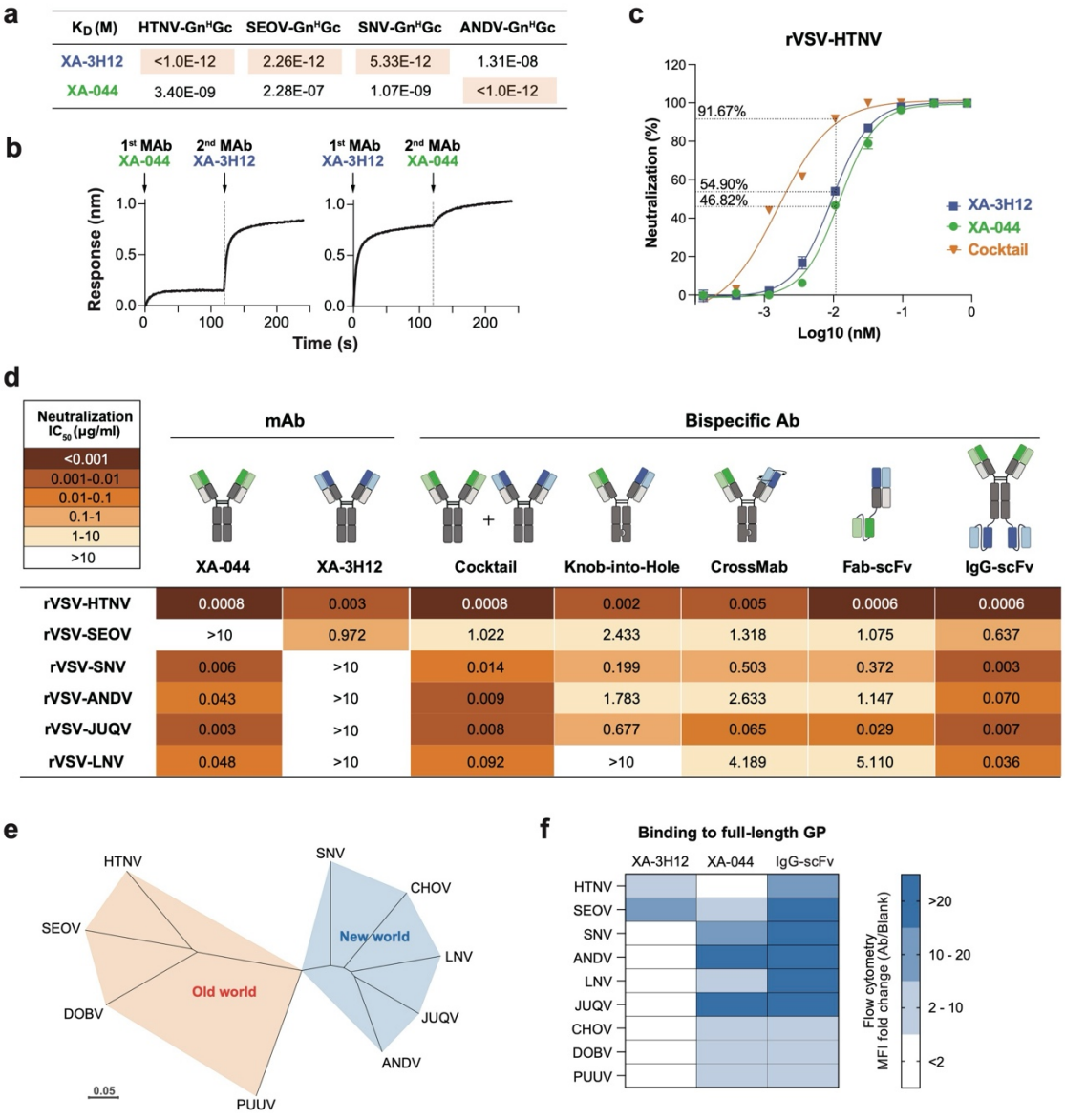

K_D (M)	HTNV-Gn^{H}Gc	SEOV-Gn^{H}Gc	SNV-Gn^{H}Gc	ANDV-Gn^{H}Gc
XA-3H12	<1.0E-12	2.26E-12	5.33E-12	1.31E-08
XA-044	3.40E-09	2.28E-07	1.07E-09	<1.0E-12

	XA-044	XA-3H12	Cocktail	Knob-into-Hole	CrossMab	Fab-scFv	IgG-scFv
rVSV-HTNV	0.0008	0.003	0.0008	0.002	0.005	0.0006	0.0006
rVSV-SEOV	>10	0.972	1.022	2.433	1.318	1.075	0.637
rVSV-SNV	0.006	>10	0.014	0.199	0.503	0.372	0.003
rVSV-ANDV	0.043	>10	0.009	1.783	2.633	1.147	0.070
rVSV-JUQV	0.003	>10	0.008	0.677	0.065	0.029	0.007
rVSV-LNV	0.048	>10	0.092	>10	4.189	5.110	0.036

Fig. 4 | Bispecific antibody strategies achieve pan-hantavirus neutralization.

a. Binding affinities of XA-3H12 and XA-044. Binding kinetics to HTNV-, SEOV-, SNV-, and ANDV-Gn^{H}Gc were measured by BLI and fit to a 1:1 Langmuir model. Affinities are reported as K_D values.

b. Competition analysis between XA-044 and XA-3H12 by BLI. Recombinant HTNV Gn^{H}Gc was saturated with the first antibody, followed by incubation with the second neutralizing antibody to assess competitive binding.

c. Synergistic neutralization by XA-044 and XA-3H12. Based on experimentally determined IC_{50} values, XA-044 (0.0051 nM) and XA-3H12 (0.0160 nM) were mixed at a 1:1 volume ratio, using their respective IC_{50} concentrations as the reference concentration (0.0106 nM). The mixture was then subjected to 3-fold serial dilutions above and below 1× and tested in standard neutralization assays. Neutralization (%) at the

combined IC_{50} concentration is indicated by dashed lines and annotated. Data represent mean ± SEM from two independent experiments.

d. Neutralization breadth and potency of parental antibodies, antibody cocktail, and bispecific antibodies. Neutralizing activities were evaluated against six hantavirus pseudoviruses. Color intensity denotes neutralization IC_{50} values across viral strains and antibody formats. Data represent mean ± SEM from two independent experiments.

e,f, Flow cytometric analysis of antibody binding to cell-surface-expressed full-length hantavirus glycoprotein (GP). **(e)** Phylogenetic analysis of representative Old World and New World hantaviruses included in the flow cytometry assay. **(f)** Heatmap summarizing antibody-binding activity, quantified by mean fluorescence intensity (MFI) from flow cytometry.

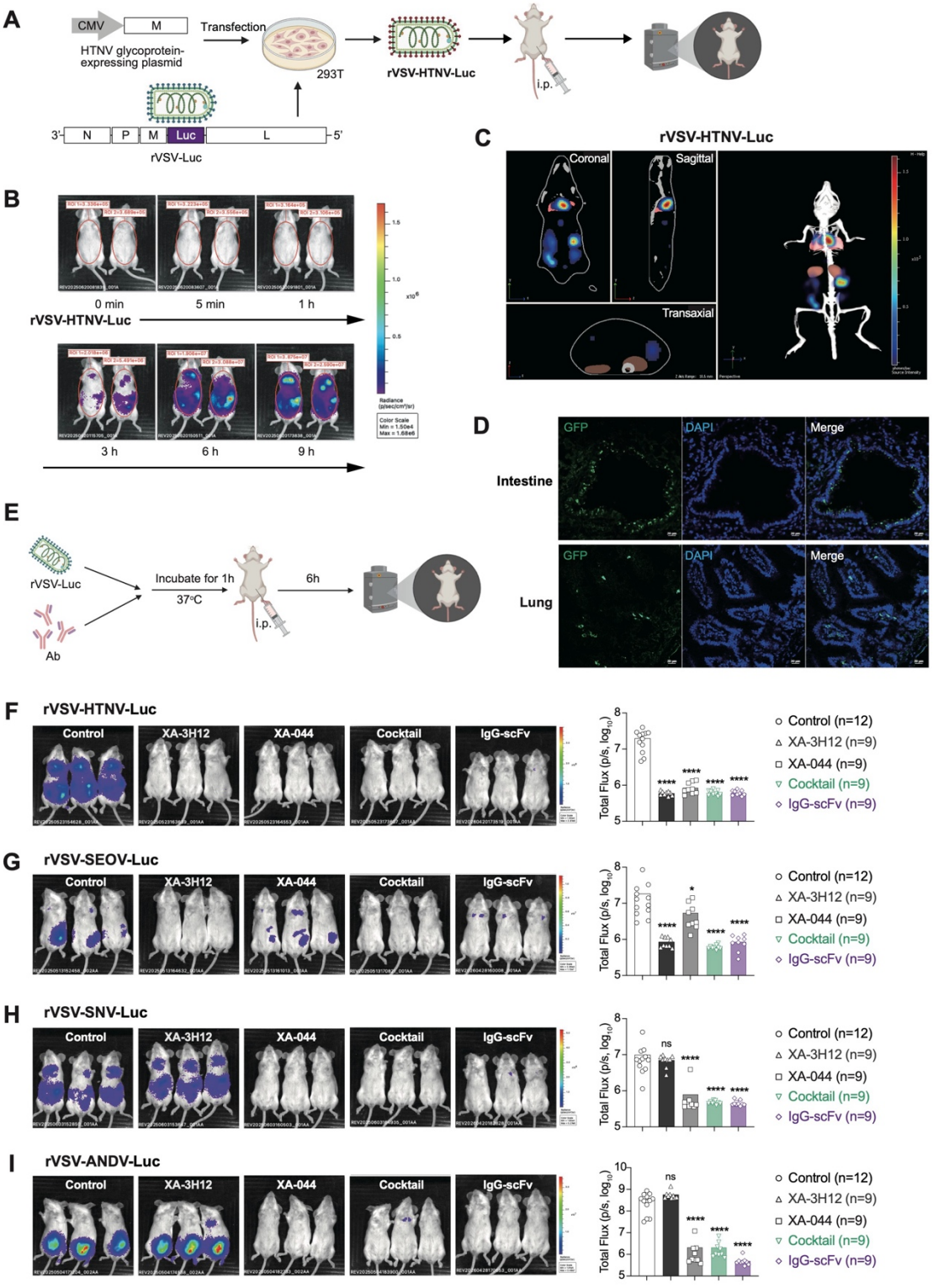

Fig. 5 | A pseudovirus reporter system enables *in vivo* evaluation of hantavirus entry blockade. **a,** Schematic of the pseudovirus *in vivo* infection model. Hantavirus glycoproteins were expressed on HEK293T cells, which were then infected with luciferase-expressing rVSV-Luc to generate rVSV-

HTNV-Luc pseudoviruses. Pseudoviruses were administered to mice by intraperitoneal (i.p.) injection, and infection was quantified by *in vivo* bioluminescence imaging.

b, Temporal dynamics of bioluminescence in rVSV-HTNV-inoculated mice. Live-animal imaging was performed at the indicated time points, with all images displayed on the same scale.

c, Representative three-dimensional bioluminescence imaging of rVSV-HTNV-inoculated mice at 6 h post-inoculation using the IVIS Spectrum system.

d, Immunofluorescence analysis of rVSV-HTNV infection in the intestine (upper panels) and lung (lower panels) collected 6 h after inoculation. GFP-expressing rVSV-Luc pseudoviruses were used. GFP-positive signals are shown in green, and nuclei were counterstained with DAPI (blue). Scale bars, 75 μm.

e-i Antibody-mediated blockade of pseudovirus entry in mice. **(e)** Experimental design. Luciferase-expressing **(f)** rVSV-HTNV-Luc, **(g)** rVSV-SEOV-Luc, **(h)** rVSV-SNV-Luc, or **(i)** rVSV-ANDV-Luc pseudoviruses were preincubated with neutralizing antibodies before i.p. administration into BALB/c mice. Bioluminescence was measured at 6 h post-inoculation. Representative images are shown on the left, with quantified bioluminescence intensities on the right. Statistical significance was determined using the Mann-Whitney test. ns, not significant; $p \geq 0.05$; *$p < 0.05$; ** $p < 0.01$; *** $p < 0.001$; **** $p < 0.0001$.

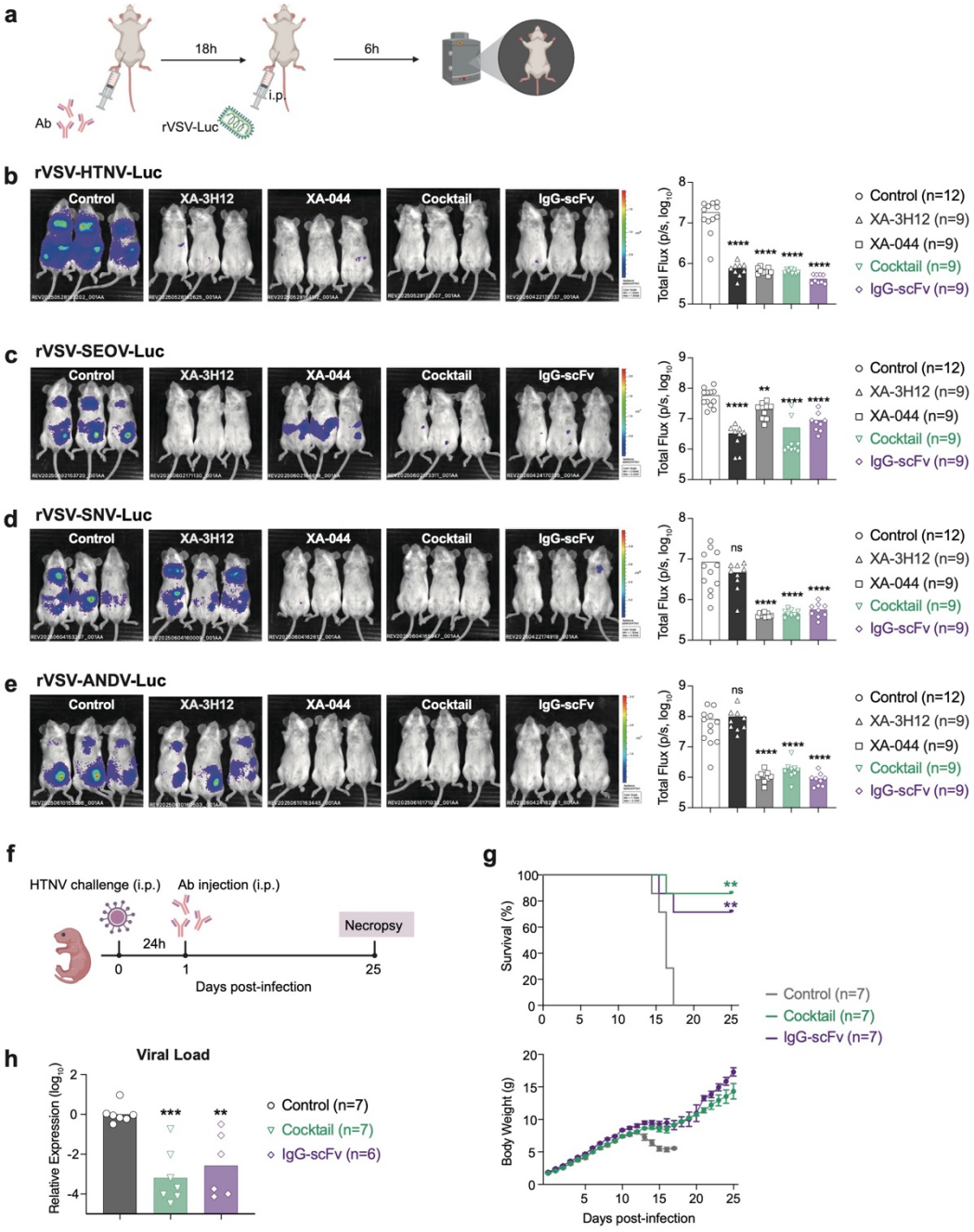

Fig. 6 | Bispecific strategies confer broad protection *in vivo.*

a-e, Prophylactic treatment prevented pseudovirus entry in mice. **(a)** Experimental design. Antibodies were i.p. administered into BALB/c mice 18 h prior to challenge with luciferase-expressing **(b)** rVSV-HTNV-Luc, **(c)** rVSV-SEOV-Luc, **(d)** rVSV-SNV-Luc, or **(e)** rVSV-ANDV-Luc pseudoviruses. Bio-luminescence was measured at 6 h post-inoculation. Representative images are shown on the left, with quantified bioluminescence intensities on the right.

f-i, Post-exposure therapy protected neonatal mice from lethal HTNV challenge. **(f)** Experimental design. Neonatal BALB/c mice were challenged i.p. with authentic HTNV and received i.p. administration of the antibody cocktail, IgG-scFv, or isotype control antibody at 24 h post-infection. **(g)** Survival curves and body weight changes. **(h)** Viral RNA loads in brain. Statistical significance was determined using the Mann-Whitney test. ns, not significant; $p \geq 0.05$; *$p < 0.05$; ** $p < 0.01$; *** $p < 0.001$; **** $p < 0.0001$.

SUPPLEMENTARY FIGURES AND FIGURE LEGENDS

a

Basic information of HFRS convalescent patients

	Gender	Age	Diagnosis date	Diagnostic criteria
Donor 1	Male	46	24 Nov 2023	HTNV IgG+
Donor 2	Male	41	24 Dec 2023	HTNV IgM+, IgG+
Donor 3	Male	19	31 Dec 2023	HTNV IgM+, IgG+
Donor 4	Male	30	7 Dec 2023	HTNV IgG+

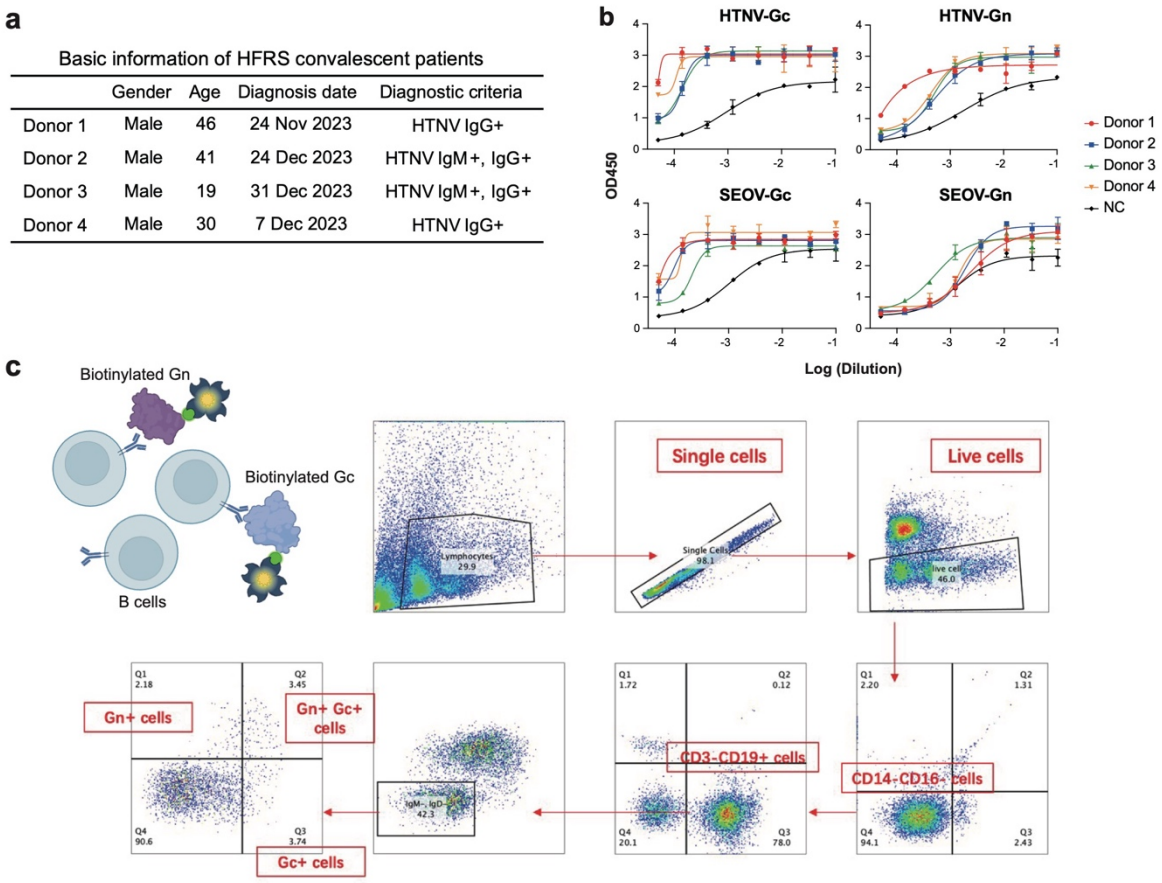

Extended Data Fig. 1 | Antigen-specific B cell sorting from HFRS convalescent donors.

a, Clinical characteristics of four HFRS convalescent donors diagnosed in 2023. Donors were confirmed to be HTNV IgG-positive and/or IgM-positive during hospitalization. Peripheral blood was collected during convalescence, approximately 6 months after discharge, after informed consent.

b, Plasma binding to HTNV and SEOV Gn and Gc from four convalescent HFRS donors was measured by ELISA. Plasma from a healthy donor was used as the negative control (NC). Data represent mean ± SEM from two independent experiments.

c, Representative flow-cytometric gating strategy for single-cell sorting of antigen-specific memory B cells recognizing HTNV-Gn, HTNV-Gc, SEOV-Gn, or SEOV-Gc.

A

Group	MAb	Donor	Heavy chain variable gene sequence					Light chain variable gene sequence				
				CDR3 length (aa)	Mutation rate (%)	V-gene and allele	J-gene and allele		CDR3 length (aa)	Mutation rate (%)	V-gene and allele	J-gene and allele
Single cell PCR	1H2	Donor 1	AKDGPIRNFGLEV	13	95.59	IGHV3-30*18	IGHJ6*02	QAWDRSTVI	9	93.80	IGLV3-1*01	IGLJ2*01
	1D4	Donor 1	ARSCYGGGCYYYYYMDV	17	94.85	IGHV1-69*09	IGHJ6*03	GTWETIQRAWV	11	94.22	IGLV1-51*01	IGLJ3*02
	4G10	Donor 4	VRDGSYCSGGSCYSTNWFDL	20	94.24	IGHV3-33*01	IGHJ5*02	TSYTSRSTVL	10	95.92	IGLV2-14*03	IGLJ2*01
	3A8	Donor 3	ARDWGWFAFDY	11	95.61	IGHV3-21*01	IGHJ4*02	VTWDDSLNGIL	11	95.56	IGLV1-44*01	IGLJ2*01
	2H5	Donor 2	ARDQTGSGWASGF	13	91.55	IGHV3-21*01	IGHJ4*02	SSYVGTNNVI	10	96.26	IGLV2-8*01	IGLJ2*01
	1A5	Donor 1	ARISSGWFGGAFDI	14	93.17	IGHV1-3*01	IGHJ3*02	QQSYSVPT	8	94.37	IGKV1-39*01	IGKJ1*01
	3H12	Donor 3	ASTPGYDTPWYGPVR	15	93.22	IGHV3-64D*06	IGHJ4*02	QKYNMAPFT	9	97.89	IGKV1-27*01	IGKJ3*01
	4E4	Donor 4	SAKDSGTWSSGVRDVFDV	18	90.97	IGHV3-53*04	IGHJ3*01	QKYNSAPWT	9	97.89	IGKV1-27*01	IGKJ1*01
	4G11	Donor 4	VCDYMWGTPLDY	12	89.09	IGHV3-53*04	IGHJ4*02	QNYDHAPRT	9	93.71	IGKV1-27*01	IGKJ1*01
	5F12	Donor 4	ARATFNYDYVWGKYRDDYLDY	21	98.30	IGHV3-33*01	IGHJ4*02	QQYNSYSRT	9	95.80	IGKV1-5*04	IGKJ1*01
Single cell BCR-seq	HT-SNY-39	/	AREAYASRTYYNNWFDP	17	85.03	IGHV4-59*01	IGHJ5*02	QSYDSSLGGSV	11	95.65	IGLV1-40*01	IGLJ3*02
	HT-SNY-44	/	ATGVRYGELHHPQYFYYGMDV	21	91.78	IGHV3-23*01,IGHV3-23*02,IGHV3-23D*01	IGHJ6*02	QQSFSPLWT	9	94.70	IGKV1-39*01,IGKV1D-39*01	IGKJ1*01
	HT-SNY-51	/	TGYCSGASCYSGPYYLDN	18	91.22	IGHV3-30*18,IGHV3-30-5*01	IGHJ4*02	QQSYSSPWT	9	94.72	IGKV1-39*01,IGKV1D-39*01	IGKJ1*01
	HT-SNY-58	/	ARDRGGQRNDNWSRFYMDV	19	91.64	IGHV4-61*02	IGHJ6*03	QQSFGTPYT	9	95.78	IGKV1-39*01,IGKV1D-39*01	IGKJ2*01
	HT-SNY-60	/	VRGFCSRTSCQRPNNYFDP	19	91.53	IGHV3-30*03,IGHV3-30*04,IGHV3-30*19	IGHJ5*02	GSYTGTSTWV	10	95.92	IGLV2-14*03	IGLJ3*02

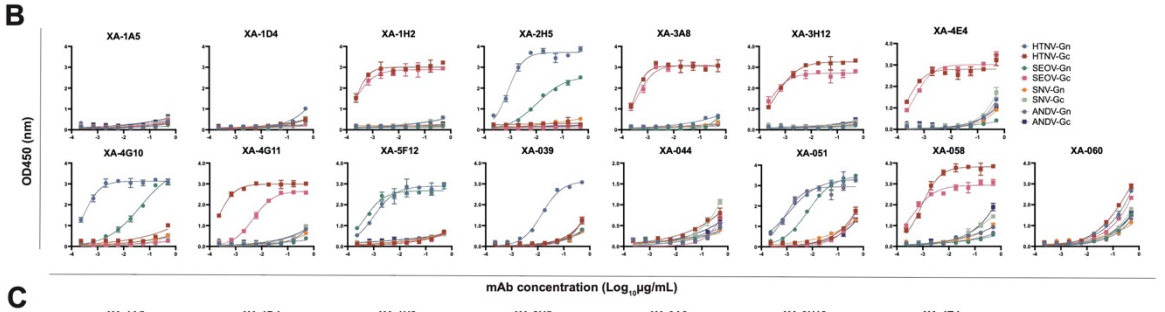

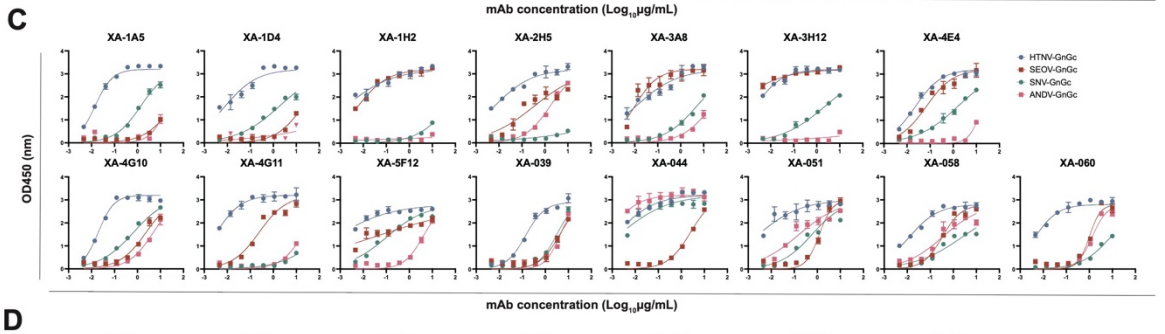

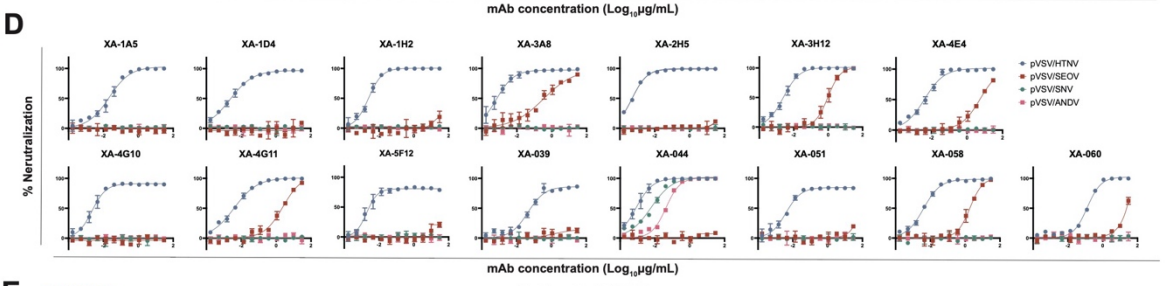

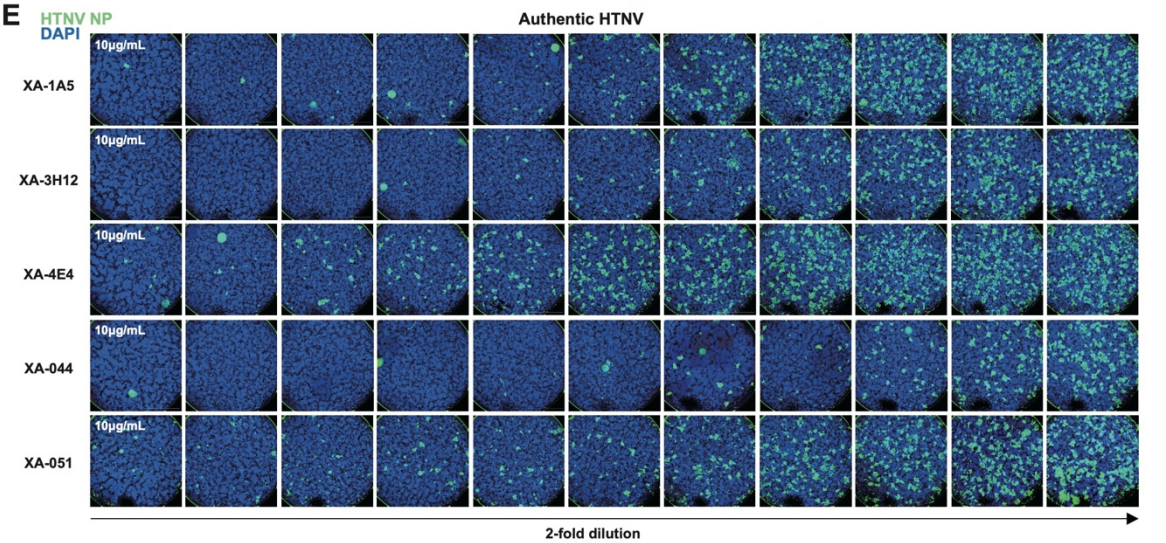

119

Extended Data Fig. 2 | Characterization of isolated neutralizing antibodies.

a, Immunogenetic features of 15 antigen-specific BCR sequences isolated from HFRS convalescent donors, including donor origin, heavy- and light-chain CDR3 amino acid sequences and lengths, somatic hypermutation frequencies, and V/J-gene usage and alleles.

b,c, Representative ELISA binding curves of isolated mAbs against recombinant Gn and Gc **(b)** or $Gn^{H}Gc$ proteins **(c)**. Data are mean ± SEM from two independent experiments; corresponding EC_{50} values are summarized in Fig. 2c.

d, Representative neutralization curves of isolated mAbs against rVSV-HTNV-GFP, rVSV-SEOV-GFP, rVSV-SNV-GFP, and rVSV-ANDV-GFP pseudoviruses. Data are mean ± SEM from two independent experiments; corresponding IC_{50} values are summarized in Fig. 2d.

e, Representative immunofluorescence images showing neutralization of authentic HTNV. Vero E6 cells were infected with HTNV (strain 76118) preincubated with neutralizing antibodies, and infection was quantified by immunofluorescent staining of HTNV Nucleocapsid protein (NP).

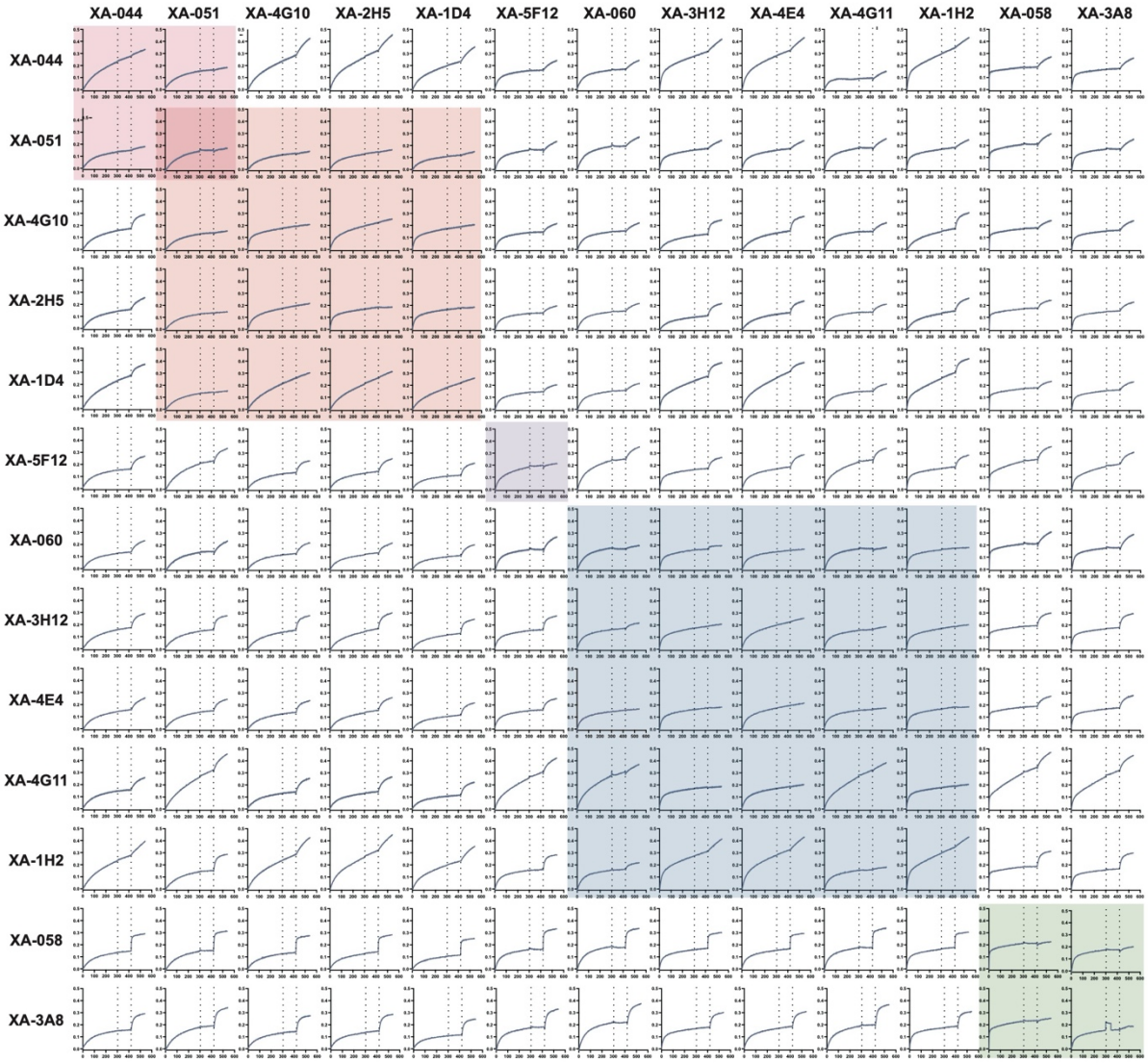

Extended Data Fig. 3 | BLI-based epitope competition analysis of neutralizing antibodies. Recombinant HTNV $Gn^{H}Gc$ protein was immobilized via binding to a primary neutralizing antibodies, followed by binding assessment of a second neutralizing antibodies. Epitope competition was quantified as the difference in response (ΔRLU) between sequential antibody-binding steps. Related to Fig. 2e.

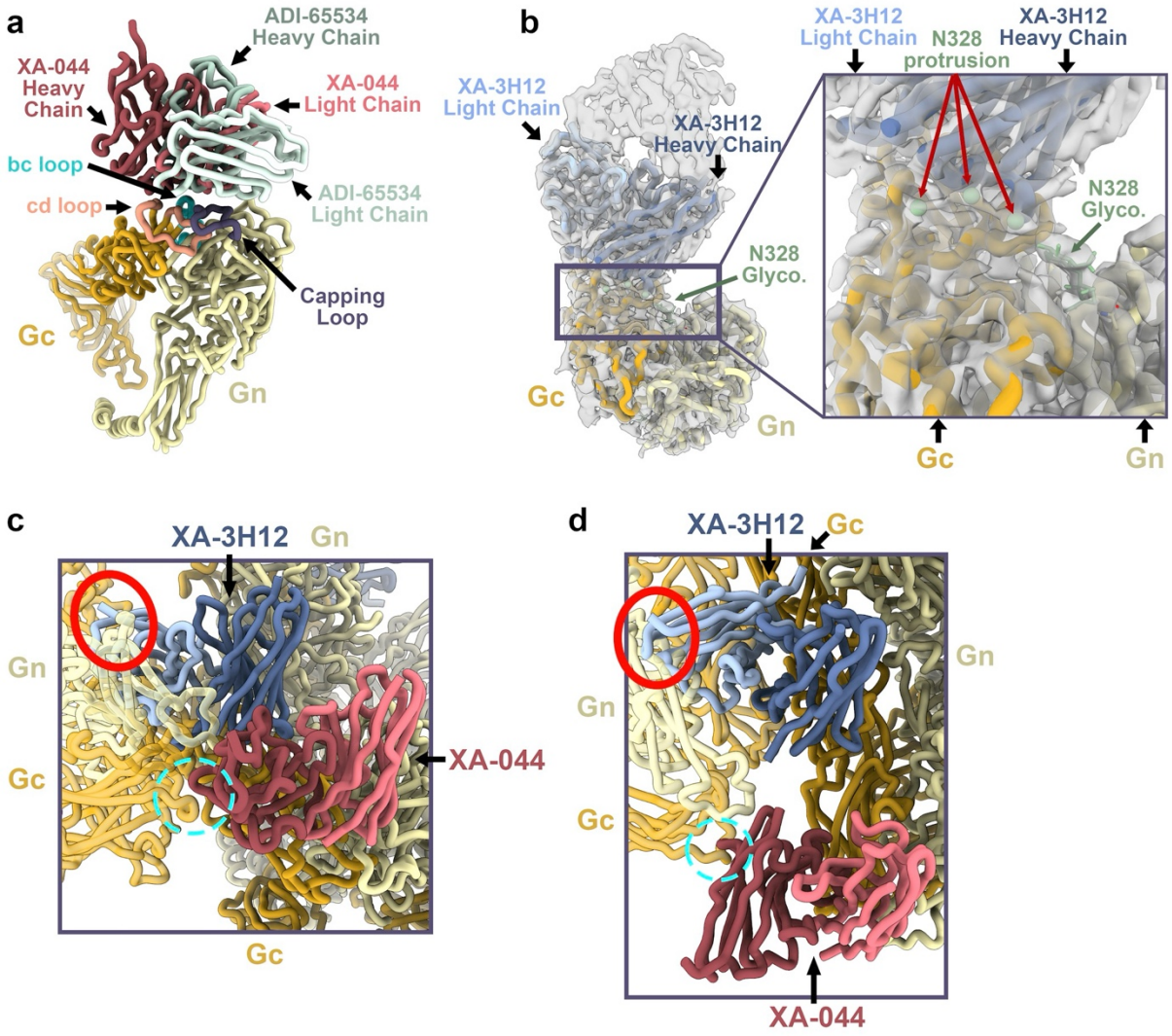

Extended Data Fig. 4 | Focused analysis of XA-044 and XA-3H12 epitopes and neutralization mechanism.

a, Superposition of XA-044 on the ANDV Gn-Gc dimer bound by ADI-65534, showing overlapping epitopes with XA-044 shifted slightly toward the Gc fusion loops (bc and cd loops). Gn: yellow, Gc: gold; XA-044 heavy and light chains: dark and light red; ADI-65534 heavy and light chains: dark and light mint; Gc bc loop: cyan, Gc cd loop: salmon.

b, The N-glycan protruding from N328 of HTNV Gn interacts with the XA-044 heavy chain. Left, overall view; right, zoomed-in view with the XA-3H12 Fab-HTNV $Gn^{H}Gc$ complex fitted into the cryo-EM density map. The purple rectangle indicates the zoomed-in region. Built glycans are shown as green sticks, and hypothesized glycan protrusions are shown as green dots.

c,d, Zoomed-in views of steric clashes between XA-044 or XA-3H12 and a neighboring Gn-Gc tetramer in the lattice, with XA-044 in red, XA-3H12 in blue, Gn in yellow, and Gc in gold. Cyan circles indicate a potential minor clash between XA-044 and the neighboring tetramer, whereas red circles indicate major clashes between XA-3H12 and the neighboring tetramer.

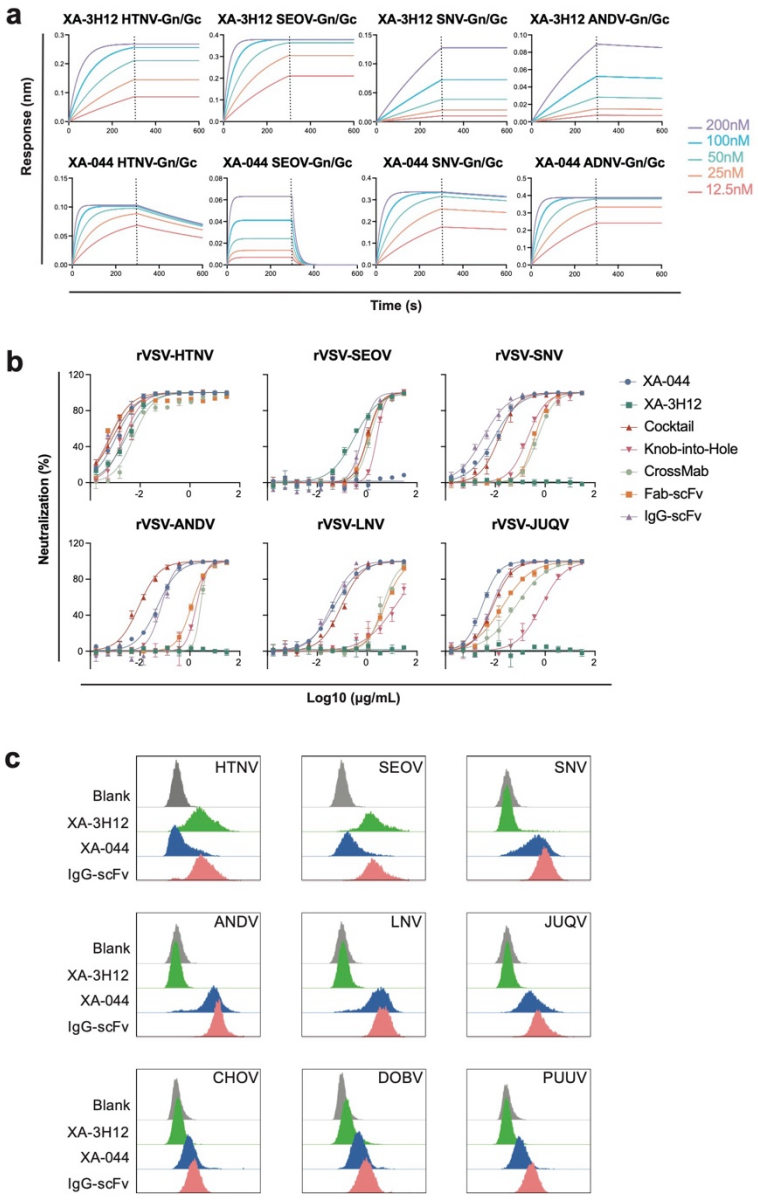

Extended Data Fig. 5 | Characterization of selected NAbs and bispecific antibodies.

a, BLI analysis of NAb binding to HTNV-, SEOV-, SNV-, and ANDV-Gn^{H}Gc. Binding kinetics were measured using 2-fold serial dilutions of recombinant Gn^{H}Gc antigens (200-12.5 nM) and fit to a 1:1 Langmuir model. Binding affinities are reported as K_D values.

b, Representative neutralization curves of parental NAbs, an antibody cocktail, and bispecific antibodies against hantavirus pseudoviruses, including rVSV-HTNV, rVSV-SEOV, rVSV-SNV, rVSV-ANDV, rVSV-JUQV, and rVSV-LNV. Data are mean ± SEM from two independent experiments; corresponding IC_{50} values are summarized in Fig. 3d.

c, Flow cytometric analysis of antibody binding to full-length hantavirus glycoprotein (GP). HEK293T cells expressing the indicated GP were incubated with individual antibodies followed by fluorophore-conjugated secondary antibody staining. Colored histograms indicate specific binding, and the gray histogram indicates the negative control. Related to Figure 3f.

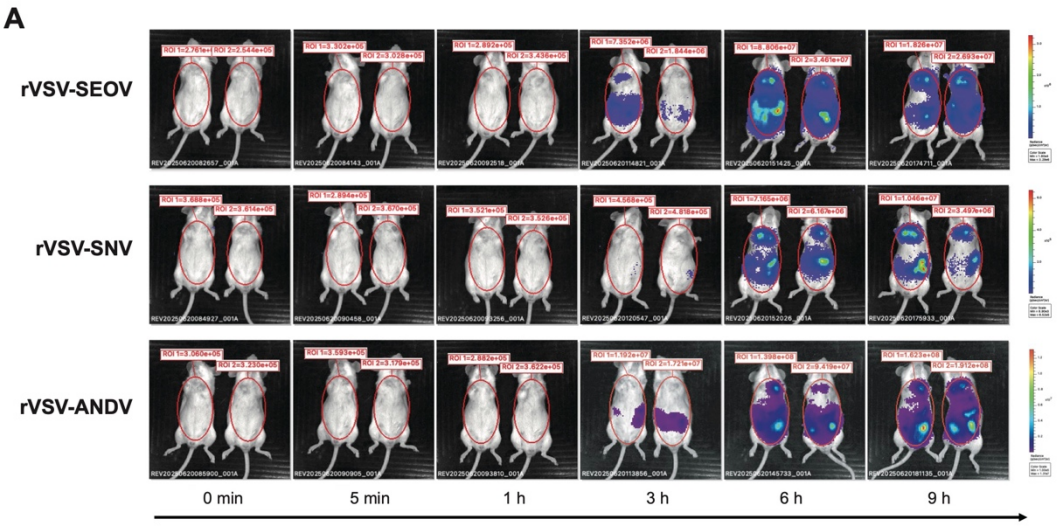
A
rVSV-SEOV
rVSV-SNV
rVSV-ANDV
0 min
5 min
1 h
3 h
6 h
9 h

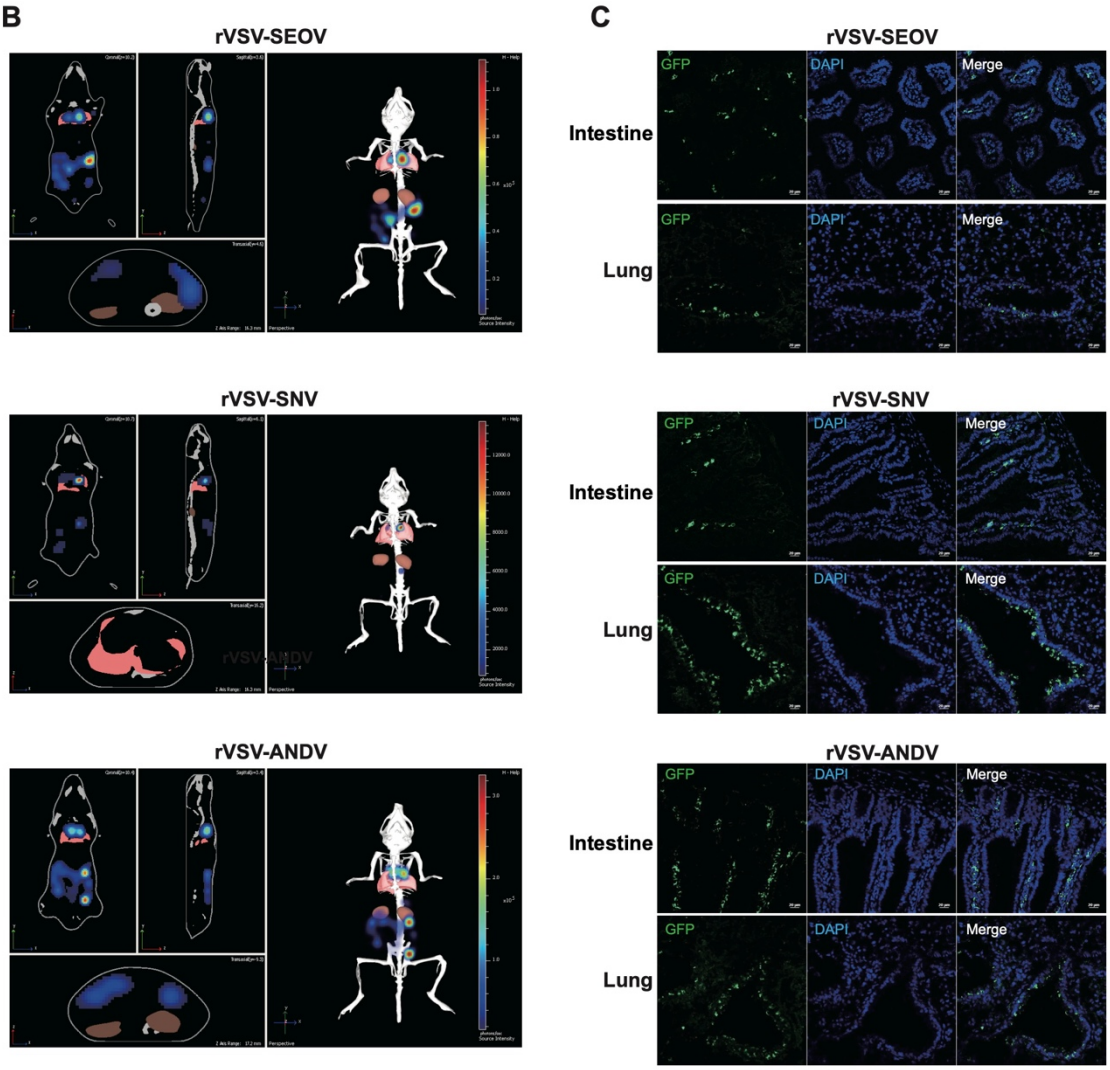
B
rVSV-SEOV
rVSV-SNV
rVSV-ANDV
C
rVSV-SEOV
rVSV-SNV
rVSV-ANDV
Intestine
Lung
GFP
DAPI
Merge

169

Extended Data Fig. 6 | Establishment of a pseudovirus-based *in vivo* infection system.

a, Temporal dynamics of bioluminescence signals in rVSV-SEOV-Luc, rVSV-SNV-Luc, and rVSV-ANDV-Luc infected mice. *In vivo* bioluminescence imaging was performed at the indicated time points after inoculation. All images were processed and displayed using the same intensity scale.

b, Representative 3D images of mice inoculated with rVSV-SEOV-Luc, rVSV-SNV-Luc, or rVSV-ANDV-Luc at 6 h post-inoculation.

c, Immunofluorescence analysis of rVSV-SEOV-GFP, rVSV-SNV-GFP, and rVSV-ANDV-GFP infection in the intestine (upper panels) and lung (lower panels) collected 6 h after inoculation. GFP-positive signals are shown in green, and nuclei were counterstained with DAPI (blue). Scale bars, 75 μm.

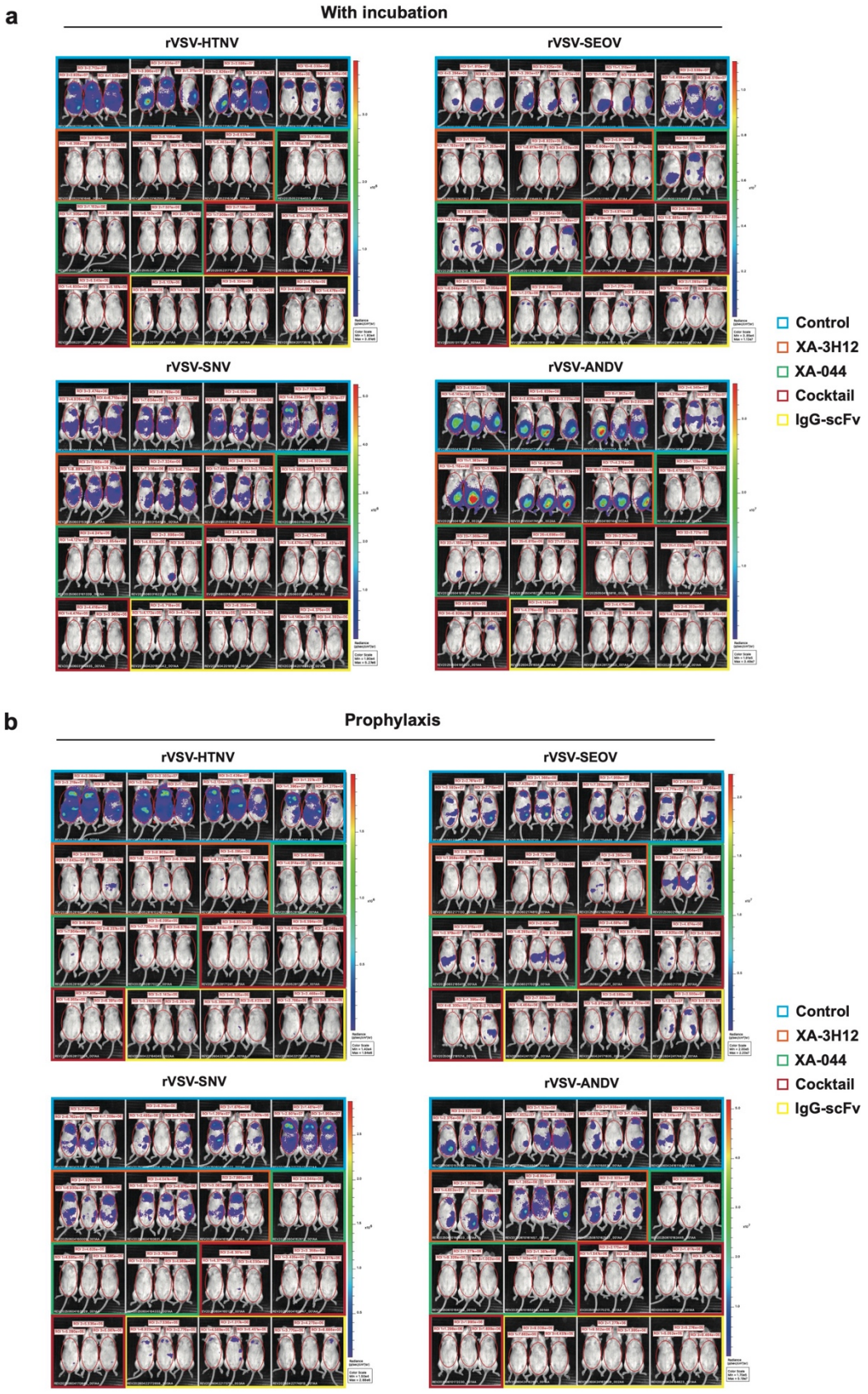
a
With incubation
rVSV-HTNV
rVSV-SEOV
rVSV-SNV
rVSV-ANDV
Control
XA-3H12
XA-044
Cocktail
IgG-scFv
b
Prophylaxis
rVSV-HTNV
rVSV-SEOV
rVSV-SNV
rVSV-ANDV
Control
XA-3H12
XA-044
Cocktail
IgG-scFv

180

Extended Data Fig. 7 | Bioluminescence imaging related to Figures 4 and 5.

a, Complete dataset for antibody-mediated blockade of pseudovirus entry shown in Fig. 4f-i.

d, Complete dataset for the prophylactic antibody protection study shown in Fig. 5b-e.

Extended Data Table 1 | Immunogenetic analysis and experimental data of the hantavirus Gn/Gc-specific antibodies.

Extended Data Table 2 | Cryo-EM data collection, processing and model refinement statistics.